

This is the author's final, peer-reviewed manuscript as accepted for publication (AAM). The version presented here may differ from the published version, or version of record, available through the publisher's website. This version does not track changes, errata, or withdrawals on the publisher's site.

Controlling Cherenkov angles with resonance transition radiation

Xiao Lin, Sajan Easo, Yichen Shen, Hongsheng Chen,
Baile Zhang, John D. Joannopoulos, Marin Soljačić
and Ido Kaminer

Published version information

Citation: X Lin et al. "Controlling Cherenkov angles with resonance transition radiation." Nature Physics, vol. 14, no. 8 (2018): 816-821.

DOI: [10.1038/s41567-018-0138-4](https://doi.org/10.1038/s41567-018-0138-4)

This version is made available in accordance with publisher policies. Please cite only the published version using the reference above. This is the citation assigned by the publisher at the time of issuing the AAM. Please check the publisher's website for any updates.

This item was retrieved from **ePubs**, the Open Access archive of the Science and Technology Facilities Council, UK. Please contact epubs@stfc.ac.uk or go to <http://epubs.stfc.ac.uk/> for further information and policies.

Controlling Cherenkov angles with resonance transition radiation

Xiao Lin^{1,2}, Sajan Easo^{3*}, Yichen Shen⁴, Hongsheng Chen¹, Baile Zhang^{2,5}, John D. Joannopoulos⁴, Marin Soljačić⁴, and Ido Kaminer⁶

¹*State Key Laboratory of Modern Optical Instrumentation, The Electromagnetics Academy at Zhejiang University, Zhejiang University, Hangzhou 310027, China.*

²*Division of Physics and Applied Physics, School of Physical and Mathematical Sciences, Nanyang Technological University, Singapore 637371, Singapore.*

³*Particle Physics Department, Rutherford-Appleton Laboratory (STFC-UKRI), Didcot, OX110QX, United Kingdom.*

⁴*Department of Physics, Massachusetts Institute of Technology, Cambridge, MA 02139, USA.*

⁵*Centre for Disruptive Photonic Technologies, NTU, Singapore 637371, Singapore.*

⁶*Department of Electrical Engineering, Technion-Israel Institute of Technology, Haifa 32000, Israel*

**email: Sajan.Easo@cern.ch*

Cherenkov radiation provides a valuable way to identify high energy particles in a wide momentum range, through the relation between the particle velocity and the Cherenkov angle. However, since the Cherenkov angle depends only on material's permittivity, the material unavoidably sets a fundamental limit to the momentum coverage and sensitivity of Cherenkov detectors. For example, Ring Imaging Cherenkov detectors must employ materials transparent to the frequency of interest as well as possessing permittivities close to unity to identify particles in the multi GeV range, and thus are often limited to large gas chambers. It would be extremely important albeit challenging to lift this fundamental limit and control Cherenkov angles *at will*. Here we propose a new mechanism that uses the constructive interference of resonance transition radiation from photonic crystals to generate both forward and backward effective Cherenkov radiation. This mechanism can control the radiation angles in a flexible way with high sensitivity to any desired range of velocities. Photonic crystals thus overcome the material limit for Cherenkov detectors, enabling the use of transparent materials with arbitrary values of permittivity, and provide a promising versatile platform well-suited for identification of particles at high energy with enhanced sensitivity.

The relation between the angle of Cherenkov radiation cones (denoted as Cherenkov angle θ below) [1,2] and the velocity v of charged particles is of fundamental importance to many applications [3-6]. For example, this determines the sensitivity of different types of Cherenkov detectors such as the Ring Image Cherenkov (RICH) detectors [7, 8] for particle identification.

However, the relation between the Cherenkov angle and the particle velocity is inherently limited by the material in which the Cherenkov radiation is emitted. This unavoidably sets a strict limit on the design of Cherenkov detectors. For conventional Cherenkov radiation generated in a nonmagnetic material, when the particle velocity is known, the Cherenkov angle relies *only* on the material's relative permittivity ϵ_r (which determines the refractive index $n = \sqrt{\epsilon_r}$) through the formula $\cos\theta = (n\beta)^{-1}$, where $\beta = \frac{v}{c}$ and c is the speed of light in free space. Regular transparent dielectrics are not suitable for conventional Cherenkov detectors. This is because these materials have a relative permittivity far above unity and the Cherenkov angle would saturate to a value independent of the particle velocity. As an example, quartz has relative permittivity around 2, limiting the useful momentum range to below 3.5 GeV/c (and even that requires using water instead of air to out-couple the light) [9]. Large volumes of gas radiators with relative permittivity very close to unity are typically used to detect particles with momentum higher than 10 GeV/c [10-12].

The limitation of Cherenkov radiation in regular transparent dielectrics also comes from another reason: the total internal reflection at the air-dielectric interface will prevent the Cherenkov radiation generated by relativistic particles from being observed for relative permittivity $\epsilon_r > 2$, as coincidentally happens for most transparent dielectrics, and especially in the visible spectrum [13]. Having $\epsilon_r > 2$ leads to the following inequality: $\lim_{v \rightarrow c} \left(\frac{\epsilon_r \omega^2}{c^2} - \frac{\omega^2}{v^2} \right)^{1/2} > \frac{\omega}{c}$ for Cherenkov radiation fields inside the dielectric, and then the fields outside the dielectric become evanescent. Besides, material losses (bulk absorption) have a large impact on the performance of Cherenkov detectors. Recently, anisotropic metal-based metamaterials with a complex permittivity, which still requires one component of the relative permittivity very close to

one, have been proposed to control Cherenkov angles [14]. However, the existence of loss, which is particularly unavoidable in metal-based system, will destroy the relation between the Cherenkov angle and the particle velocity, as described in Supplementary Section 4. Therefore, it shall be necessary to use purely transparent systems to gain efficient control of the Cherenkov angle.

The studies of Cherenkov radiation and its applications have a long history [3-6, 15-19], and recently there is renewed interest and progress in the topic [20-29]. But the ability to control the Cherenkov angle in a flexible way is still limited by the permittivity of the radiator material as described above and remains very challenging.

In this paper, we propose a new underlying mechanism for the generation of Cherenkov radiation from a one-dimensional (1D) photonic crystal composed of widely-available transparent dielectrics, which can transmit into air and thus can be used in Cherenkov detector designs like the RICH. This comes from the constructive interference of the forward or backward resonance transition radiation from periodic dielectric interfaces. Therefore, along with the availability of many lossless dielectrics and the flexibility in the design of periodic structures [30], this mechanism allows photonic crystals to flexibly control both the forward and backward Cherenkov angles. We note that while many phenomena based on Cherenkov radiation have been studied in photonic crystals [22, 27, 31], including the backward (or reversed) Cherenkov radiation [20], spectroscopy of photonic nanostructures [3], and novel compact radiation sources [4, 17-19], the possibility of using photonic crystals to tailor the Cherenkov angle has not been directly addressed. In addition, the proposed Cherenkov detectors based on photonic crystals are different from transition radiation detectors [32], where the latter relies only on the intensity of transition radiation from multilayer structures and disregards the information of radiation angles [33-35].

To illustrate the underlying physics, we begin by schematically showing in Fig. 1 that the effective Cherenkov radiation can be generated by the constructive interference of resonance transition radiation excited from multiple interfaces in 1D photonic crystals. The simplest 1D photonic crystal can be constructed by alternating two different dielectric materials with relative permittivities denoted as ϵ_{r1} and

ϵ_{r2} that are taken to be transparent (lossless); the impact of loss on the effective Cherenkov radiation from photonic crystals is described in Supplementary Section 6. When the relativistic particle with a charge of q and a velocity of $\bar{v} = \hat{z}\beta c$ penetrates through a 1D photonic crystal, forward (backward) radiation can be generated in the bottom (top) air region, as shown in Fig. 1a. As a conceptual demonstration of resonance transition radiation, Fig. 1b presents the radiation field distribution (without the charge field) generated from a swift electron ($\beta = 0.5022$) passing through a 1D photonic crystal ($\epsilon_{r1} = 2$ and $\epsilon_{r2} = 2.3$).

Resonance transition radiation from 1D photonic crystals is analytically calculated by extending Ginzburg and Frank's theory of transition radiation [34, 35] to a 1D photonic crystal structure; the detailed calculations are in Supplementary Sections 1-2. Since the particle velocity is below the Cherenkov threshold, i.e. $\beta < [\max(\epsilon_{r1}, \epsilon_{r2})]^{-1/2}$, there will be no conventional Cherenkov radiation within each dielectric. However, due to the transition radiation at each interface, plane-like waves are still emitted within the photonic crystal near the particle trajectory, as Fig. 1b clearly shows. Interestingly, the z-component of the Poynting's vector S (which represents the direction of power flow) is antiparallel to the direction of motion of the particle. Consequently, more radiation energy enters into the top air region than into the bottom air region. These are characteristic features of the effective backward Cherenkov radiation, which originates entirely from the constructive interference of resonance transition radiation in the backward direction. This new mechanism for the generation of Cherenkov radiation is different from that of conventional Cherenkov radiation described by the theory developed by Frank and Tamm [2, 33] and from that of Smith-Purcell radiation [36, 37]. For the latter two cases, the generated fields are directly emitted into the air region without the intermediate modulation by a periodic dielectric environment, and the charged particle moves only within one material without crossing interfaces between different materials.

We would like to emphasize that all the radiation into air in the photonic crystal designs we propose, comes only from the interference of resonance transition radiation. When the resonance transition radiation interferes constructively in air, it behaves similar to the conventional Cherenkov radiation. In this sense, such resonance transition radiation can be treated as the effective Cherenkov radiation of photonic crystal

Bloch modes that can couple out to air, and whose phase velocity is smaller than the particle velocity; this is elaborated in Supplementary Section 6. In contrast, when the resonance transition radiation interferes destructively in air, it behaves similar to the conventional transition radiation, and is devoid of the characteristic features of the Cherenkov radiation (because the corresponding Bloch modes that get emitted cannot couple out to air and are trapped inside the photonic crystal by total internal reflection). Importantly, the Cherenkov angles from photonic crystals can be sensitive to relativistic particle velocities as shown in Fig. 1c-g.

The resonance transition radiation from 1D photonic crystals can be devised for manipulating the effective Cherenkov angles. To gain an intuitive understanding of such schemes, we qualitatively analyze the interaction between the charged particle and the eigenmodes of the photonic crystal. When the particle is assumed to move along the z -direction, it induces a current density of $\bar{J}^q(\bar{r}, t) = \hat{z} \frac{qv}{2\pi\rho} \delta(z - vt)\delta(\rho)$ in cylindrical coordinates [34, 35, 38]. By transforming all quantities to the frequency domain, we have the particle-induced fields proportional to $\exp(i\frac{\omega}{v}z)$ [34, 35, 38], at each angular frequency ω . From the momentum-matching condition, the charged particle is prone to excite the eigenmodes of photonic crystals with the wavevector along the z -direction being $k_z = \frac{c}{v} \cdot \frac{\omega}{c}$ [17]. Moreover, in order to guarantee that the excited modes inside the photonic crystal can reach the detectors – which are generally located in the air region (or more generally, in an external medium) – we need to avoid the total internal reflection at the photonic crystal-air interface. This requires the wavevector along the ρ -direction of the excited modes being $k_\rho \leq \frac{\omega}{c}$. Due to the momentum matching along the ρ -direction at the photonic crystal-air interface, k_ρ determines the Cherenkov angle θ in the air region, i.e., $k_\rho = \frac{\omega}{c} \sin(\theta)$.

From the above analysis, the relation between the Cherenkov angle in air and the particle velocity is effectively determined by the isofrequency contour of photonic crystals at each frequency, i.e., the relation between the wavevectors k_z and k_ρ . Two representative kinds of conceptual isofrequency contours of photonic crystals are shown in Fig. 2; practical examples such contours can be seen in Supplementary

Section 5. As the particle velocity increases in the range $[v_{min}, v_{max}]$, the Cherenkov angle in air increases in the range $[\theta_{min}, \theta_{max}]$ in Fig. 2a, but decreases in the range $[\theta_{max}, \theta_{min}]$ in Fig. 2b.

Controlling Cherenkov angles using these two schemes in Fig. 2 are illustrated in Fig. 3 and Fig. 4. In these figures, the working wavelength in air is set to be 700 nm, and the relative permittivities of the two dielectric constituents of the photonic crystals configured are set to be $\epsilon_{r1} = 10.6$ (such as GaP) and $\epsilon_{r2} = 2.1$ (SiO₂) [13]. Here, although the charge particles can create conventional Cherenkov radiation inside each dielectric layer, those photons remain trapped by total internal reflection at the dielectric-air interface and cannot contribute to radiation in the air. This is because the conventional Cherenkov radiation emerges with $k_\rho = \frac{\omega}{c} \sqrt{\epsilon_r - \beta^{-2}}$ [33] that satisfies the condition of total internal reflection $k_\rho > \frac{\omega}{c}$ (here $\epsilon_r > 2$ and $\beta \rightarrow 1$). In these figures, the forward (backward) angular spectral energy density $U(\lambda, \theta) = \frac{dW}{d\omega d\Omega}$ [34, 35, 38], which represents the energy W radiated per unit angular frequency ω per unit solid angle Ω ($d\Omega = 2\pi \sin\theta d\theta$), is adopted to characterize the forward (backward) radiation in the bottom (top) air region shown in Fig.1; more details are in Supplementary Section 3.

Figure 3 illustrates the first scheme of controlling Cherenkov angles as proposed in Fig. 2a. Figures 3a,b show the angular spectral energy density from the photonic crystal. The resulting radiation energy in the air region flows predominantly along paths such that in each case the corresponding radiation angle is highly dependent on the particle velocity. Moreover, the forward radiation energy in Fig. 3a is ~100 times larger than the backward radiation energy in Fig. 3b. Therefore, the resonance transition radiation from this photonic crystal can be effectively considered as the forward Cherenkov radiation. The weak backward radiation in Fig. 3b is attributed to the mostly-destructive interference of resonance transition radiation in the backward direction.

Although conventional transition radiation has no threshold for the particle velocity, the resonance transition radiation that constructively interferes in air has a threshold for the particle velocity $v_{threshold}$ (as described in Supplementary Section 6.6), which in Fig. 3a is $v_{threshold} = 0.99c$. The appearance of

such a threshold emphasizes the deep connection of this particular resonance transition radiation with the effective Cherenkov radiation of the Bloch modes. Altogether, the radiation into air can be classified into two regimes, i.e., Cherenkov-like radiation when $v > v_{threshold}$ and (non-resonance) transition-like radiation when $v < v_{threshold}$. These two categories of radiation can also be distinguished from their radiation spectra, as delineated in Supplementary Section 6.7. Here, for particle identification, we utilize the radiation with $v > v_{threshold}$.

The Cherenkov angle from photonic crystals is well-suited for high-energy particle identification. For example, by applying the angle-velocity relation of Fig. 3a, we show the relation between the particle momentum and the Cherenkov angle for four types of particles in Fig. 3c. Here, for the hypothesis of the particle being electron, pion, kaon or proton with a momentum of 6.6 GeV/c, the corresponding Cherenkov angles are 10.3°, 10.2°, 8.7° or 0°, respectively. This would enable the different particle types to be effectively distinguished from one another in the region near this momentum. As another example, Fig. 3d shows the use of photonic crystals for particle identification at very high momenta (~500 GeV/c). It may also be noted that, as with conventional radiators, Cherenkov angles for all particle types in Fig. 3c,d tend to converge as the particles' momenta increase to large values (as described in Supplementary Section 6), thus requiring to have different photonic crystal designs for different momentum ranges.

Figure 4 shows the second scheme of controlling Cherenkov angles as proposed in Fig. 2b. The backward radiation energy in Fig. 4b is ~10 times larger than the forward radiation energy in Fig. 4a. This is attributed to the constructive (destructive) interference of resonance transition radiation in the backward (forward) direction. Here also, the angular spectral energy density in air shows that the radiation angles are sensitive to the particle velocity. As a schematic demonstration of the effective backward Cherenkov radiations, the far field distribution of radiation from an electron with different velocities highlighted by yellow dots in Fig. 4b are shown in Fig. 1c-g. Figure 4c shows the relation between the Cherenkov angles and the particle momenta for backward Cherenkov radiation from photonic crystals. In this figure, for particles with a fixed momentum of 4 GeV/c (20 GeV/c), the Cherenkov angles corresponding to electron,

pion, kaon and proton hypothesis are 0° , 2.6° , 9.5° and 18° (0° , 0.48° , 1.88° and 3.58°), respectively. From this one can infer that this scheme is also suitable for identification of high energy particles and that it can be used in different momentum ranges.

These two schemes above help to surmount the limitations posed by conventional radiators. For example, to cover the momentum range 1-10 GeV/c, there is a dearth of suitable conventional materials with permittivity around 1.06. The silica aerogels [12] which are typically used for this, suffer from significant losses due to Rayleigh scattering. To cover high momenta near 500 GeV/c would require using a gas at extremely low density and such a Cherenkov detector is difficult to operate.

While the forward Cherenkov radiation has been extensively studied [9, 10], the backward Cherenkov radiation [39] has never been considered for the design of Cherenkov detectors. When photonic crystal is used for backward Cherenkov radiation in the second scheme, the emitted photon and the particle are naturally separated in opposite directions and hence their physical interference is minimized. This can lead to Cherenkov detector designs with two radiators for two different momentum ranges where the emitted photons go in forward or backward directions depending on the momentum of the charged particle. Such designs would reduce the hit occupancy in the corresponding photon detector planes and thus improve the particle identification performance, compared to the configuration where all the photons go forward and reach a single photon detector plane. As another illustration, since the difference between Cherenkov angles from electron and pion in Fig. 4c is much larger than that in Fig. 3c, the second scheme may offer a better precision in distinguishing between these particles than the first scheme and what is achievable from conventional radiators.

In order to facilitate the potential design of Cherenkov detectors based on photonic crystals, some of the salient features of the effective Cherenkov radiation from photonic crystals are described below. The number of photons emitted per unit length from the photonic crystal described in this paper is similar to that from anisotropic metamaterials in Ref. [14], but is one order of magnitude smaller than what could be achieved from an isotropic material of hypothetical similar refractive index as can be inferred from Fig. 3a

and Supplementary Sections 3 and 4. One option to increase the photon yield is to increase the thickness of the crystal. Various options to increase the yield are described in Supplementary Section 7. The fraction of the effective Cherenkov radiation emitted into the relevant direction is over 75% as shown in Supplementary Section 6.

The prospect of a thin photonic structure for the design of Cherenkov detectors is highly desirable because the gas radiators used for particle identification above 10 GeV/c are typically at least one meter long. Using photonic crystals, the radiator length may be reduced to few millimeters, considering that such crystals will have ~ 10000 periods, with the potential to create sufficient number of photons. The constraint in increasing the number of layers is that the amount of radiation energy loss introduced by the photonic crystal should be small enough to keep a low rate of secondary particle production. This would require using transparent dielectric materials made from combinations of materials with low atomic number like silicon, oxygen, carbon, and nitrogen. One also needs to ensure that the material used is radiation hard so that its properties do not degrade when used in a high radiation environment like the particle detector regions of the Large Hadron Collider (LHC).

We also note that using photonic crystals to design Cherenkov detectors might suffer from the chromatic aberration induced by the periodic structure. This also happens for Cherenkov detectors from anisotropic metal-based metamaterials [14], due to the high frequency dispersion of the permittivity in metals. The chromatic aberration will cause the Cherenkov angle to be sensitive to the frequency. Mitigating the chromatic effect is part of optimizing the photonic crystal design for a particular Cherenkov detector and some options for this are summarized below. They are described in more detail, in Supplementary Section 6.

A simple option is to use filters to limit the frequency range and to compensate for corresponding reduction in photon yield, the number of layers may be increased. Another option is to limit the maximum momentum envisaged for particle identification from a given photonic crystal. For example, for the photonic crystal structure used in Fig. 3c, when the particle momentum is less than 3 GeV/c, the impact of

chromatic aberration is negligible. A different approach is to measure the time of arrival of the photons on the detector plane to infer its wavelength and apply the required correction to the angle as described in [40]. This method makes use of the variation in group velocity coming from the variation in wavelength of the photons produced.

A general approach, which minimizes the chromatic aberration inside the photonic crystal, is to use gain materials with anomalous dispersion [41-43] to construct the photonic crystal, since the material's anomalous dispersion can help to cancel the dispersion caused by the periodic structure. In Supplementary Section 6, this is elucidated with a numerical example for the 1-16 GeV/c range. The usage of such gain materials may also help to augment photon yield while keeping the radiator thin, since the photons emitted will be amplified during their propagation.

Alternately, the usage of optical elements (such as the achromatic doublets) to apply such corrections, as done in many microscopes [44, 45], is also worth exploring. Moreover, the anisotropy in the crystal in the plane normal to the charged track direction, may also help to magnify the Cherenkov angles produced [14] and thus reduce the effect of chromatic aberrations. After applying the correction to chromatic aberration using such approaches, the bandwidth can potentially be extended to over several tens to a few hundreds of nm, depending on the photonic crystal design and the dielectric materials used. The potential for such approaches are evinced with numerical examples in Supplementary Section 6.

It is also important to note that typical Cherenkov detectors receive particles along different trajectories. In experiments like those at the LHC, several high energy particles are produced in the region near the nominal interaction point of the beam particles, and then they move outward from that region. For example, the particles produced in the pseudorapidity range from 2 to 5 (i.e, travelling within a cone of about 300 mrad around the axis of collision), would be incident at small angles on a flat plane of the photonic crystal. For such cases, corrections can be applied to the above formalism [34] to estimate the Cherenkov angle. One can also design the photonic crystal such that it forms a spherical segment to facilitate normal incidence of a large fraction of such particles and thus minimize any such corrections. Since the

radius of curvature of such a segment is much larger than the structural periodicity, we can consider the curved crystal as effectively a planar structure to a very good approximation. The fabrication of such a structure is different from that of conventional 1D photonic crystals. Nevertheless, a number of viable approaches already exist as indicated in Supplementary Section 7. These include multilayer polymer sheets (used as 1D photonic crystals in a number of applications [46-48]) that can be easily bent.

During the production of photonic crystals, one can deposit layers so that the required thickness of each layer can be attained with single-nanometer precision over large areas (tens of cm² and even square meters, e.g. [49, 50]). Some of the options available for this in the industry, are described in Supplementary Section 7.

To conclude, this paper introduces a new mechanism, i.e. the constructive interference of resonance transition radiation in the forward or backward direction, to generate the Cherenkov radiation from a 1D photonic crystal. This new mechanism allows to control both the forward and backward Cherenkov angles in a flexible way, despite using transparent dielectrics with their relative permittivities far above unity, and thus overcomes the material limit for the design of conventional Cherenkov detectors. In particular, the Cherenkov angle from photonic crystal can be engineered to be suitable for particle identification in very different momentum ranges, some of which cannot be achieved with conventional radiator materials. With the combined advantages of the abundant choice of dielectrics and the flexibility in the structural design, photonic crystals thus provide a new viable platform for the design of Cherenkov detectors with enhanced sensitivity and for the design of novel radiation sources.

Methods

Methods, including statements of data availability and any associated accession codes and references, are available at <https://doi.org/xx.xxxx/sxxxxx-xxx-xxxx-x>.

References

- [1] Cherenkov, P. A. Visible emission of clean liquids by action of gamma radiation. *Dokl. Akad. Nauk SSSR* **2**, 451-454 (1934).
- [2] Frank, I. M. & Tamm, I. *Dokl. Akad. Nauk SSSR* **14**, 109-114 (1937).
- [3] de Abajo, F. J. G. et al. Cherenkov effect as a probe of photonic nanostructures. *Phys. Rev. Lett.* **91**, 143902 (2003).

- [4] Adamo, G. et al. Light well: A tunable free-electron light source on a chip. *Phys. Rev. Lett.* **103**, 113901 (2009).
- [5] Cook, A. M. et al. Observation of narrow-band terahertz coherent Cherenkov radiation from a cylindrical dielectric-lined waveguide. *Phys. Rev. Lett.* **103**, 095003 (2009).
- [6] Liu, F. et al. Integrated Cherenkov radiation emitter eliminating the electron velocity threshold. *Nat. Photon.* **11**, 289-292 (2017).
- [7] Galbraith, W. & Jelley, J. V. Light pulses from the night sky associated with cosmic rays. *Nature* **171**, 349-350 (1953).
- [8] Ypsilantis, T. & Seguinot, J. Theory of ring imaging Cherenkov counters. *Nucl. Instrum. Meth. A* **343**, 30-51 (1994).
- [9] Adam, I. et al. The DIRC particle identification system for the BaBar experiment. *Nucl. Instrum. Meth. A* **538**, 281-357 (2005).
- [10] Alves Jr, A. A. et al. (LHCb Collaboration). The LHCb detector at the LHC. *JINST* **3**, S08005 (2008).
- [11] Adinolfi, M. et al. (LHCb RICH collaboration). Performance of the LHCb RICH at the LHC. *Eur. Phys. J. C* **73** (2013), 2431.
- [12] Abashian, A. et al. The Belle detector. *Nucl. Instrum. Meth. A* **478**, 117-232 (2002).
- [13] Palik, E. D. *Handbook of Optical Constants of Solids* (Academic, New York, 1985).
- [14] Ginis, V., Danckaert, J., Veretennicoff, I. & Tassin, P. Controlling Cherenkov radiation with transformation-optical metamaterials. *Phys. Rev. Lett.* **113**, 167402 (2014).
- [15] Chamberlain, O., Segrè, E., Wiegand, C. & Ypsilantis, T. Observation of antiprotons. *Phys. Rev.* **100**, 947-950 (1955).
- [16] Aubert, J. J. et al. Experimental observation of a heavy particle J. *Phys. Rev. Lett.* **33**, 1404-1406 (1974).
- [17] Liu, S. et al. Surface Polariton Cherenkov Light Radiation Source. *Phys. Rev. Lett.* **109**, 153902 (2012).
- [18] Wong, L. J., Kaminer, I., Ilic, O., Joannopoulos, J. D. & Soljačić, M. Towards graphene plasmon-based free-electron infrared to X-ray sources. *Nat. Photon.* **10**, 46-52 (2016).
- [19] Denis, T. et al. Coherent Cherenkov radiation and laser oscillation in a photonic crystal. *Phys. Rev. A* **94**, 053852 (2016).
- [20] Luo, C., Ibanescu, M., Johnson, S. G. & Joannopoulos, J. D. Čerenkov radiation in photonic crystals. *Science* **299**, 368-371 (2003).
- [21] Xi, S. et al. Experimental verification of reversed Čerenkov radiation in left-handed metamaterials. *Phys. Rev. Lett.* **103**, 194801 (2009).
- [22] de Abajo, F. J. G. Optical excitations in electron microscopy. *Rev. Mod. Phys.* **82**, 209-275 (2010).
- [23] Vorobev, V. V. & Tyukhtin, A. V. Nondivergent Čerenkov radiation in a wire metamaterial. *Phys. Rev. Lett.* **108**, 184801 (2012).
- [24] Ren, H., Deng, X., Zheng, Y., An, N. & Chen, X. Nonlinear Čerenkov radiation in an anomalous dispersive medium. *Phys. Rev. Lett.* **108**, 223901 (2012).
- [25] Genevet, P. et al. Controlled steering of Čerenkov surface plasmon wakes with a one-dimensional metamaterials. *Nat. Nanotech.* **10**, 804-809 (2015).
- [26] Shi, X. et al. Caustic graphene plasmons with Kelvin angle. *Phys. Rev. B* **92**, 081404(R) (2015).
- [27] Kaminer, I. et al. Quantum Čerenkov radiation: Spectral cutoffs and the role of spin and orbital angular momentum. *Phys. Rev. X* **6**, 011006 (2016).
- [28] Hummelt, J. S. et al. Coherent Čerenkov-cyclotron radiation excited by an electron beam in a metamaterial waveguide. *Phys. Rev. Lett.* **117**, 237701 (2016).
- [29] Duan, Z. et al. Observation of the reversed Čerenkov radiation. *Nat. Commun.* **8**, 14901 (2017).
- [30] Joannopoulos, J., Johnson, S., Winn, J., & Meade, R. *Photonic Crystals: Molding the Flow of Light* (Princeton University Press, Princeton, NJ, 2011).
- [31] Zhang, Y. et al. Nonlinear Čerenkov radiation in nonlinear photonic crystal waveguides. *Phys. Rev. Lett.* **100**, 163904 (2008).
- [32] Andronic, A. & Wessels, J. P. Transition radiation detectors. *Nucl. Instrum. Meth. A* **666**, 130-147 (2012).
- [33] Jackson, J. D. *Classical Electrodynamics* (John Wiley & Sons, 1999).

- [34] Ginzburg, V. L. & Tsytovich, V. N. *Transition Radiation and Transition Scattering* (CRC Press, 1990).
- [35] Ginzburg, V. L. & Tsytovich, V. N. Several problems of the theory of transition radiation and transition scattering. *Phys. Rep.* **49**, 1-89 (1979).
- [36] Smith, S. J. & Purcell, E. M. Visible light from localized surface charges moving across a grating. *Phys. Rev.* **92**, 1069 (1953).
- [37] Kaminer, I. et al. Spectrally and spatially resolved Smith-Purcell radiation in plasmonic crystals with short-range disorder. *Phys. Rev. X* **7**, 011003 (2017).
- [38] Lin, X. et al. Splashing transients of 2D plasmons launched by swift electrons. *Sci. Adv.* **3**, e1601192 (2017).
- [39] Chen, H. & Chen, M. Flipping photons backward: reversed Cherenkov radiation. *Materials Today* **14**, 34-41 (2011).
- [40] Dey, B. et al. Design and performance of the Focusing DIRC detector, *Nucl.Instrum.Meth. A* **775**, 112-131 (2015).
- [41] Fang, A., Koschny, Th., Wegener, M. & Soukoulis, C. M. Self-consistent calculation of metamaterials with gain. *Phys. Rev. B* **79**, 241104(R) (2009).
- [42] Wuestner, S., Pusch, A., Tsakmakidis, K. L., Hamm, J. M. & Ortwin Hess, Overcoming losses with gain in a negative refractive index metamaterial. *Phys. Rev. Lett.* **105**, 127401 (2010).
- [43] Wang, Y. T., et al. Gain-assisted hybrid-superlens hyperlens for nano imaging. *Opt. Exp.* **20**, 22953-22960 (2012).
- [44] Batson, P. E., Dellby, N. & Krivanek, O. L. Sub-ångstrom resolution using aberration corrected electron optics. *Nature* **418**, 617-620 (2002).
- [45] Kidger, M. J. *Fundamental optical design* (SPIE press, 2002).
- [46] Liu, R. Y. F. et al. Forced assembly of polymer nanolayers thinner than the interphase. *Macromolecules* **38**, 10721-10727 (2005).
- [47] Pursiainen, O. L. J. et al. Compact strain-sensitive flexible photonic crystals for sensors. *Appl. Phys. Lett.* **87**, 101902 (2005).
- [48] Arsenault, A. C., Puzzo, D. P., Manners, I. & Ozin, G. A. Photonic-crystal full-colour displays. *Nat. Photon.* **1**, 468-472 (2007)
- [49] Sheinfux, H. H., et al. Observation of Anderson localization in disordered nanophotonic structures. *Science* **356**, 953-956 (2017).
- [50] Shen, Y. et al. Optical broadband angular selectivity. *Science* **343**, 1499-1501 (2014).

Acknowledgements

This work was sponsored by the National Natural Science Foundation of China (Grants No. 61625502, 61574127 and 61601408), the ZJNSF (LY17F010008), the Top-Notch Young Talents Program of China, the Fundamental Research Funds for the Central Universities, the Innovation Joint Research Center for Cyber-Physical-Society System, Nanyang Technological University for NAP Start-Up Grant, the Singapore Ministry of Education (Grant No. MOE2015-T2-1-070, MOE2016-T3-1-006, and Tier 1 RG174/16 (S)), and the US Army Research Laboratory and the US Army Research Office through the Institute for Soldier Nanotechnologies (Contract No. W911F-18-2-0048 and W911F-13-D-0001). I. Kaminer is an Azrieli Fellow, supported by the Azrieli foundation, and was partially supported by the Seventh Framework Programme of the European Research Council (FP7-Marie Curie IOF) under Grant No. 328853-MC-BSiCS. S. Easo is a staff member of STFC (which is a constituent part of UKRI) in U.K.

Author contributions

X.L., I.K. and S.E. initiated the idea; X.L. performed the calculation; X.L., S.E., Y.S., H.C., B.Z., J.D.J., M.S. and I.K. analyzed data, interpreted detailed results and contributed extensively to the writing of the manuscript; I.K., S.E., H.C., B.Z., J.D.J. and M.S. supervised the project.

Competing interests

The authors declare no competing financial interests.

Additional information

Supplementary information is available for this paper at <https://doi.org/xx.xxxx/sxxxx-xxx-xxxx-z>.

Reprints and permissions information is available at www.nature.com/reprints.

Correspondence and requests for materials should be addressed to S.E.

Publisher's note: Springer Nature remains neutral with regard to jurisdictional claims in published maps and institutional affiliations.

Methods

Advantage of using photonic crystals to control Cherenkov radiation. Using the two schemes described in the text, photonic crystals can control forward and backward Cherenkov angles, while conventional radiator materials, such as aerogels, gases, or anisotropic metal-based metamaterials, can control only the forward Cherenkov angle [9, 10, 14]. Moreover, photonic crystals do not suffer from the strict limitations on the available values of dielectric permittivities, and instead overcome this material limit since they enable the use of transparent materials with arbitrary values of permittivity for the design of Cherenkov detectors.

Derivation of resonance transition radiation. Resonance transition radiation from 1D photonic crystals, which are composed by isotropic materials, is rigorously calculated by extending Ginzburg and Frank's theory of transition radiation within the framework of macroscopic electrodynamics. Since we mainly consider the case with β very close to one, the high-energy particle can safely pass through the photonic crystal and its velocity is treated as constant.

In Supplementary Sections 1-2, an analytical expression of the radiated fields induced by a swift charged particle is obtained. By applying the Sommerfeld integration [38], numerical calculation of the field distribution of resonance transition radiation is carried out as shown in Fig. 1.

Based on these radiation fields, the angular spectral energy densities of photons emitted in the top and bottom air regions shown in Fig. 1, are derived in Supplementary Section 3. The angular spectral energy density from an isotropic slab is shown in Supplementary Fig. 3 and that from a photonic crystal is shown in Fig. 3, Fig. 4 and Supplementary Fig. 4. Since Maxwell equations are scalable, one can scale the wavelength by any factor and keep the same radiation characteristics (such as those in Figs. 3 and 4), as long as the structure of the photonic crystal scales by the same factor. We note that when the particle velocity increases, the radiation energy of the backward Cherenkov radiation decreases in Fig. 4b (see also Fig. 1c-g), while that of the forward Cherenkov radiation increases as in Fig. 3a.

The transition radiation from the interface between an isotropic material and a uniaxial material is also derived by using Ginzburg and Frank's theory of transition radiation. By following the principle of resonance transition radiation between isotropic materials, further derivation of the resonance transition radiation between uniaxial materials and the transition radiation from a uniaxial slab, is carried out in Supplementary Section 4. The angular spectral energy density from a uniaxial slab is shown in Supplementary Fig. 5, where the influence of material losses on the relation between the Cherenkov angle and the particle velocity is discussed.

Various features of Cherenkov radiation in our proposed photonic crystal designs. These are provided in Supplementary Section 6, including: the impact of local disorders in photonic crystals (Supplementary

Section 6.1 and Supplementary Fig. 7), angular spread of Cherenkov radiation (Supplementary Section 6.2 and Supplementary Fig. 8), and momentum range for particle identification (Supplementary Section 6.3). The equivalence between the effective Cherenkov radiation into Bloch modes and the resonance transition radiation that constructively interferes in air are discussed in Supplementary Section 6.4. The radiation mechanism is further elaborated in Supplementary Section 6.5 and Supplementary Fig. 9, by presenting the phase velocity of the excited Bloch modes that can couple out to air.

Additional supplemental studies include the exploration of the velocity threshold in our mechanisms (Supplementary Section 6.6 and Supplementary Fig. 10), the similarity between radiation spectra from our photonic crystal designs and a dielectric slab (Supplementary Section 6.7 and Supplementary Figs. 11 and 12), the bandwidth and chromatic aberration correction of Cherenkov radiation from photonic crystal (Supplementary Section 6.8 and Supplementary Figs. 13-18), the angular spectral energy density and the angle-integrated radiation spectrum at a fixed velocity (Supplementary Section 6.9), the fraction of Cherenkov radiation emitted into the desired direction (Supplementary Section 6.10), and the impact of loss in material on our mechanism of Cherenkov radiation from photonic crystals (Supplementary Section 6.11 and Supplementary Fig. 19).

Photonic crystals. The band structure and isofrequency contour of the proposed 1D photonic crystal designs are calculated in Supplementary Section 5; see Supplementary Fig. 6.

Production and usage of photonic crystals in high energy physics experiments. These are provided in Supplementary section 7. This section includes the references to the various methods available in the industry for the production of large area photonic crystals and flexible photonic crystals (Supplementary Section 7.1) and the options to increase the photon yield obtained from photonic crystals (Supplementary Section 7.2).

Data availability. The data that support the plots within this paper and other findings of this study are available from the corresponding author upon reasonable request.

Figure Captions

Fig. 1 | Schematic of controlling Cherenkov angles with photonic crystals. **a**, Structural schematic. The forward (backward) radiation is collected in the bottom (top) air region. **b-g**, Field distribution of backward Cherenkov radiation induced by the constructive interference of resonance transition radiation in the backward direction. In **b**, plane-like waves are excited near the particle trajectory (dashed green arrow), with the z -components of both the Poynting's vector S and phase velocity v_p being antiparallel to the direction of motion of the particle. In **c-g**, the Cherenkov angle is shown by the phase fronts of the far field in the top air region, exhibiting high sensitivity to the particle velocity $v = \beta c$. Here, and in the following figures, the working wavelength in air $\lambda = 2\pi c/\omega$ is set to be 700 nm. In **b**, the photonic crystal consists of 40 unit cells; the thickness of the unit cell is $d_{unit} = 0.9346\lambda$; within each unit cell, the thicknesses for the two dielectric constituents are $d_1 = d_2 = 0.5d_{unit}$; $\epsilon_{r1} = 2$ and $\epsilon_{r2} = 2.3$. In **c-g**, the thickness of the photonic crystal is 2 mm, with $d_{unit} = 0.2792\lambda$, $d_1 = 0.6d_{unit}$, $d_2 = 0.4d_{unit}$, $\epsilon_{r1} = 10.6$ and $\epsilon_{r2} = 2.1$.

Fig. 2 | Two conceptual schemes of controlling forward and backward Cherenkov angles with photonic crystals. Hypothetical isofrequency contours of photonic crystals, i.e. the relation between wavevectors k_ρ and k_z , determines the relation between the Cherenkov angle in air ($\theta = \text{asin}(\frac{k_\rho}{\omega/c})$) and the particle velocity ($\frac{v}{c} = \frac{\omega/c}{k_z}$). The goal of the two schemes is to create a wide range of Cherenkov angles for a narrow range of the particle velocity. The maximum Cherenkov angle corresponds to the maximum particle velocity in the first scheme in **a**, and corresponds to the minimum particle velocity in the second scheme in **b**.

Fig. 3 | Controlling Cherenkov angles with photonic crystals using the first scheme proposed. a,b, Angular spectral energy density of forward (backward) radiation in the bottom (top) air region. The highly directional radiation in **a** shows the relation between the Cherenkov angle and the particle velocity. **c** Cherenkov angles versus the particle momenta for four types of particles, where the velocity in **a** is converted to the momentum using the masses of the different particles. The thickness of the photonic crystal is 2 mm, with $d_{unit} = 1.0205\lambda$, $d_1 = 0.3d_{unit}$, $d_2 = 0.7d_{unit}$, $\epsilon_{r1} = 10.6$ and $\epsilon_{r2} = 2.1$. **d** Cherenkov angles versus the particle momenta, where $d_{unit} = 1.0144\lambda$ and the other parameters are the same as those in **c**. The results in this figure follow the proposed scheme in Fig. 2a.

Fig. 4 | Controlling Cherenkov angles with photonic crystals using the second scheme proposed. a,b, Angular spectral energy density of forward (backward) radiation in the bottom (top) air region. The highly directional radiation in **b** shows the relation between the Cherenkov angle and the particle velocity. Cherenkov angles at five different particle velocities, denoted as yellow dots in **b**, are schematically shown by the far field radiation in the top air region in Fig. 1c-g. **c**, Cherenkov angles versus the particle momenta for four kinds of particles, where the velocity in **b** is converted to the momentum using the masses of the different particles. The thickness of the photonic crystal is 2 mm, with $d_{unit} = 0.2792\lambda$, $d_1 = 0.6d_{unit}$, $d_2 = 0.4d_{unit}$, $\epsilon_{r1} = 10.6$ and $\epsilon_{r2} = 2.1$. The results in this figure follow the proposed scheme in Fig. 2b.

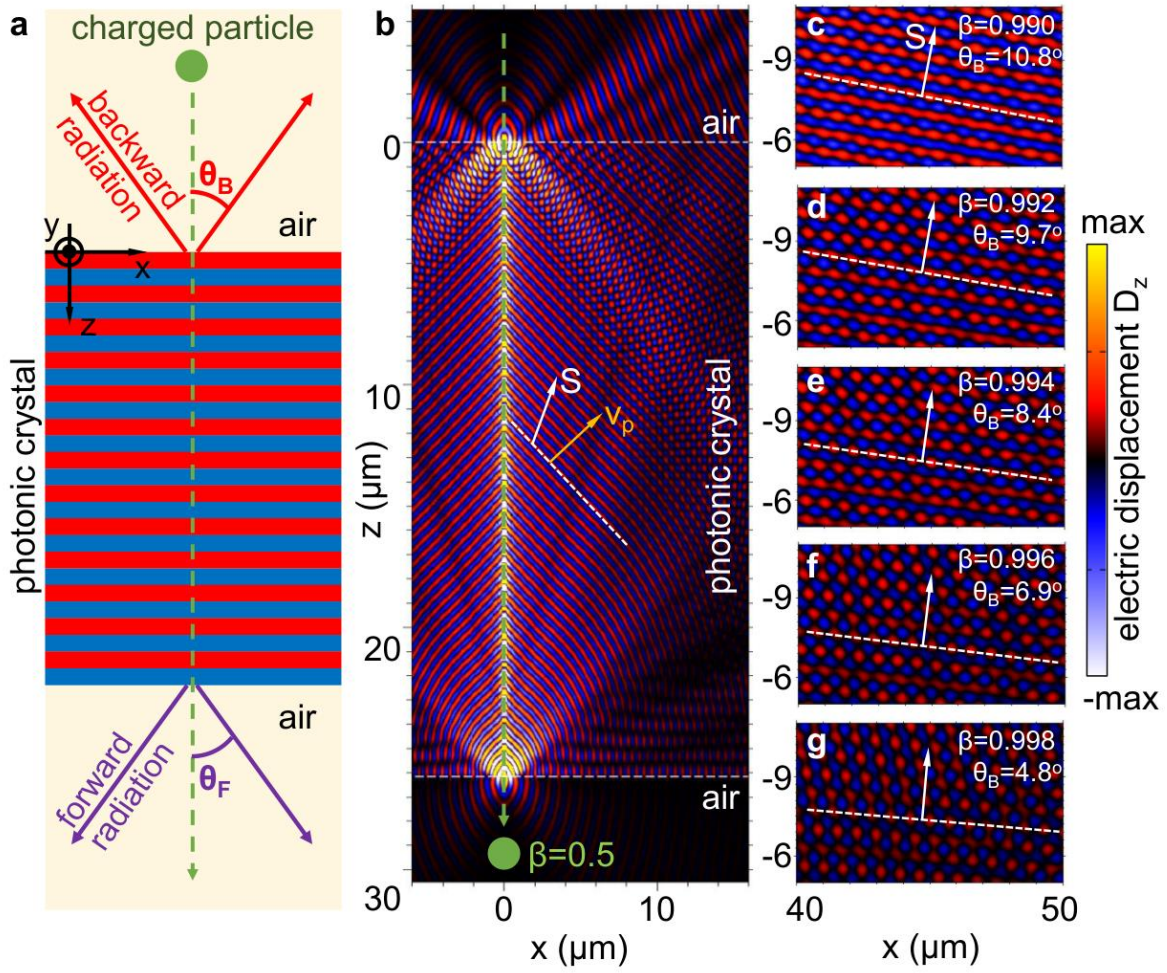


Figure 1

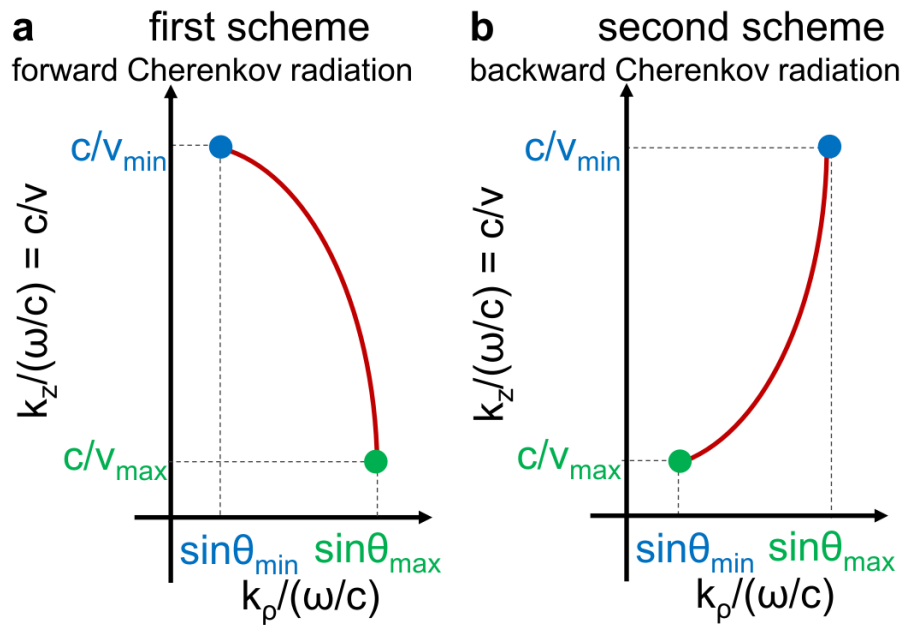


Figure 2

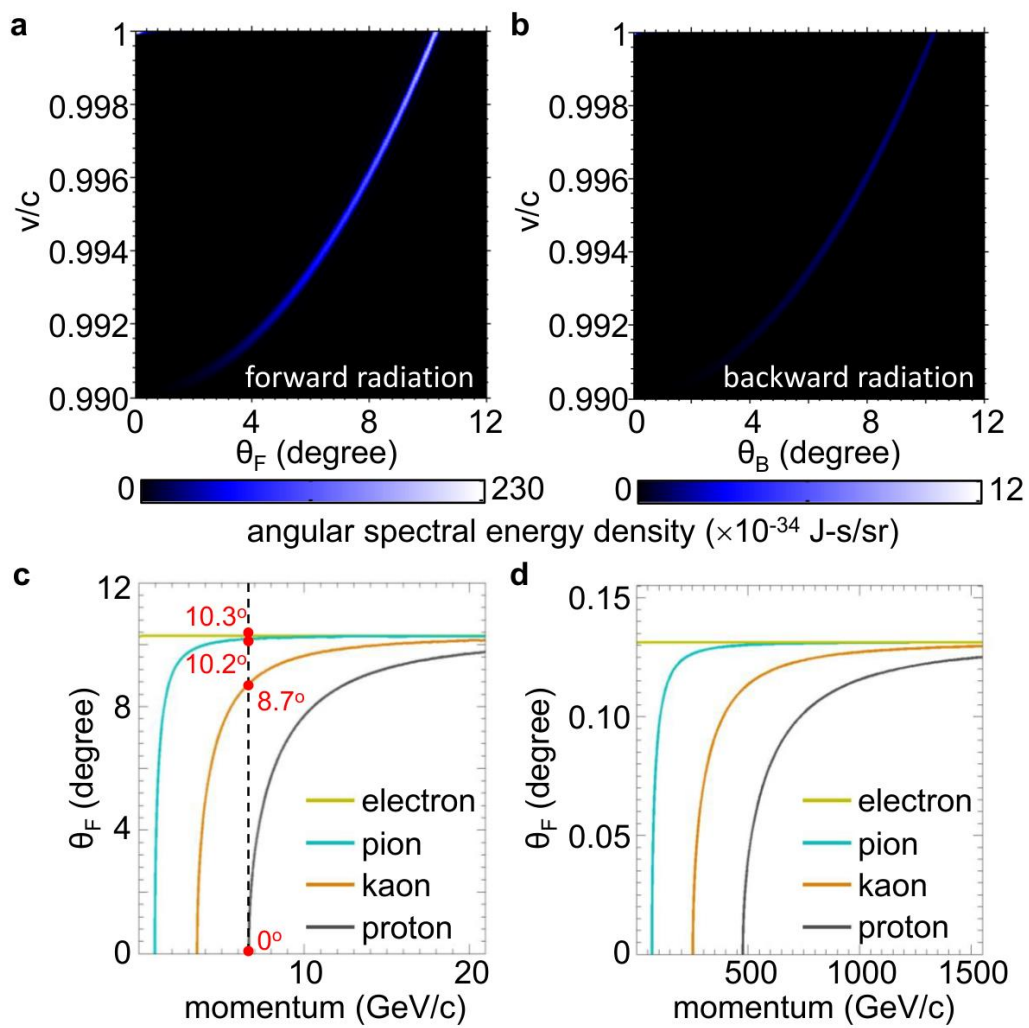


Figure 3

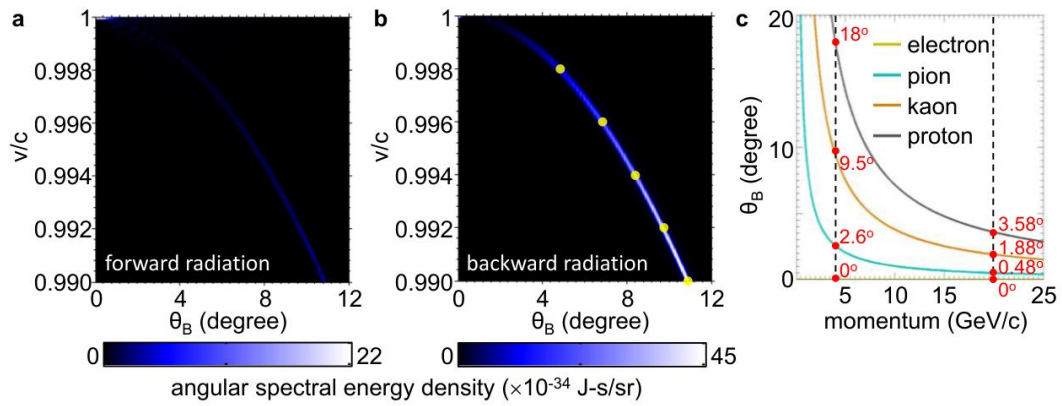
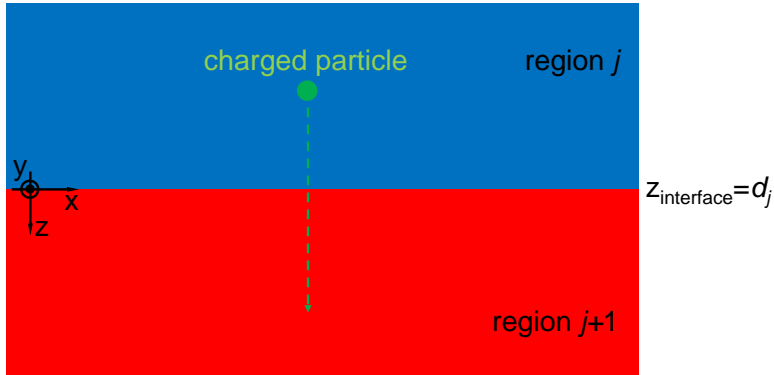


Figure 4

Supplementary Information for “Controlling Cherenkov angles with resonance transition radiation”

Supplementary section 1: Transition radiation from a single interface

We begin with the analysis of transition radiation from a charged particle perpendicularly crossing a single interface between two different isotropic regions; see Supplementary Fig. 1. The swift particle with a charge of q propagates along the $+z$ direction with a velocity of v . The two regions are denoted as region j and region $j + 1$, and have a relative permittivity of $\epsilon_{r,j}$ and $\epsilon_{r,j+1}$, respectively, where j is a positive integer. The corresponding plane of the interface between these two regions is at $z = d_j$. The detailed analytical calculation of transition radiation for the case with $d_j = 0$ has been extensively studied [22, 34, 35, 38], including that in our recent work [38]. For the convenience of following discussions, we briefly introduce the calculation procedure of transition radiation for the case with arbitrary d_j below [38].



Supplementary Fig. 1 | Structural schematic of transition radiation when a charged particle perpendicularly crosses a single interface.

Within the framework of classical electrodynamics, the current density induced by a swift charged particle is [34, 35]:

$$\vec{J}^q(\vec{r}, t) = \hat{z}qv\delta(x)\delta(y)\delta(z - vt) \quad (1)$$

By decomposing all the quantities in Fourier components in time and in the coordinates $\vec{r}_\perp = \hat{x}x + \hat{y}y$ perpendicular to the moving charge's trajectory, one has

$$\vec{J}^q(\vec{r}, t) = \hat{z}J_z^q(\vec{r}, t) = \hat{z} \int j_{\vec{k}_\perp, \omega}^q(z) e^{i(\vec{k}_\perp \cdot \vec{r}_\perp - \omega t)} d\vec{k}_\perp d\omega \quad (2)$$

$$\bar{E}(\bar{r}, t) = \int \bar{E}_{\bar{\kappa}_\perp, \omega}(z) e^{i(\bar{\kappa}_\perp \cdot \bar{r}_\perp - \omega t)} d\bar{\kappa}_\perp d\omega, \quad \bar{H}(\bar{r}, t) = \int \bar{H}_{\bar{\kappa}_\perp, \omega}(z) e^{i(\bar{\kappa}_\perp \cdot \bar{r}_\perp - \omega t)} d\bar{\kappa}_\perp d\omega \quad (3)$$

where $\bar{\kappa}_\perp = \hat{x}\kappa_x + \hat{y}\kappa_y$. From equations (1-2), one obtains $j_{\bar{\kappa}_\perp, \omega}^q(z) = \frac{q}{(2\pi)^3} e^{i\frac{\omega}{v}z}$. Below we will mainly use the fields (such as $j_{\bar{\kappa}_\perp, \omega}^q$, $\bar{E}_{\bar{\kappa}_\perp, \omega}$ and $\bar{H}_{\bar{\kappa}_\perp, \omega}(z)$) in the Fourier decomposition. For the sake of simplicity, we will not give the indices $\bar{\kappa}_\perp$ and ω for the corresponding Fourier components. By solving Maxwell equations, one can find the following equation for E_z (the component along the charge's trajectory):

$$\frac{\partial^2}{\partial z^2} (\varepsilon_r E_z) + \varepsilon_r \left(\frac{\omega^2}{c^2} \varepsilon_r - \kappa_\perp^2 \right) E_z = -\frac{i\omega\mu_0 q}{(2\pi)^3} \left(\varepsilon_r - \frac{c^2}{v^2} \right) e^{i\frac{\omega}{v}z} \quad (4)$$

where ε_r is the relative permittivity (i.e. $\varepsilon_r = \varepsilon_{r,j}$ or $\varepsilon_{r,j+1}$); ε_0 and μ_0 is the permittivity and the permeability of free space, respectively; c is the speed of light in free space. Equation (4) can be solved in each region, and the solutions should be joined by matching the boundary conditions at $z = d_j$, i.e.

$$\hat{n} \times (\bar{E}_{\perp,j} - \bar{E}_{\perp,j+1})|_{z=d_j} = 0, \quad \hat{n} \times (\bar{H}_{\perp,j} - \bar{H}_{\perp,j+1})|_{z=d_j} = 0 \quad (5)$$

where $\hat{n} = -\hat{z}$, and \bar{J}_s is the surface current density. Such a solution will be a sum of a field induced by the charge in a homogeneous medium (E_z^q) and the freely radiated field (E_z^R) [34, 35], i.e. $E_z = E_z^q + E_z^R$, where

$$E_{z,j}^q = \frac{-iq}{\omega\varepsilon_0(2\pi)^3} \frac{1 - \frac{c^2}{v^2\varepsilon_{r,j}}}{\left(\varepsilon_{r,j} - \frac{c^2}{v^2} - \frac{\kappa_\perp^2 c^2}{\omega^2}\right)} e^{i\frac{\omega}{v}z} \quad (6-1)$$

$$E_{z,j+1}^q = \frac{-iq}{\omega\varepsilon_0(2\pi)^3} \frac{1 - \frac{c^2}{v^2\varepsilon_{r,j+1}}}{\left(\varepsilon_{r,j+1} - \frac{c^2}{v^2} - \frac{\kappa_\perp^2 c^2}{\omega^2}\right)} e^{i\frac{\omega}{v}z} \quad (6-2)$$

$$E_{z,j}^R = \frac{iq}{\omega\varepsilon_0(2\pi)^3} \cdot a_{j|j+1}^- \cdot e^{-ik_{z,j}z} \quad (7-1)$$

$$E_{z,j+1}^R = \frac{iq}{\omega\varepsilon_0(2\pi)^3} \cdot a_{j|j+1}^+ \cdot e^{+ik_{z,j+1}z} \quad (7-2)$$

where the component of the wavevectors for the radiated fields along the z direction are $k_{z,j} = \sqrt{\frac{\varepsilon_{r,j}\omega^2}{c^2} - \kappa_\perp^2}$ and

$k_{z,j+1} = \sqrt{\frac{\varepsilon_{r,j+1}\omega^2}{c^2} - \kappa_\perp^2}$, respectively. Both the backward radiated field in equation (7-1) and the forward radiated field in equation (7-2) propagate away from the interface. By matching the boundary conditions, one can obtain the two radiation factors $a_{j|j+1}^-$ and $a_{j|j+1}^+$ for the radiation fields in region j and region $j + 1$, i.e.

$$a_{j|j+1}^- = a_{j|j+1}^{-,0} e^{+ik_{z,j}d_j} e^{i\frac{\omega}{v}d_j} \quad (8)$$

$$a_{j|j+1}^+ = a_{j|j+1}^{+,o} e^{-ik_{z,j+1}d_j} e^{i\frac{\omega}{v}d_j} \quad (9)$$

$$a_{j|j+1}^{-,o} = \frac{\frac{v}{c} \frac{\kappa_1^2 c^2}{\omega^2 \varepsilon_{r,j}} (\varepsilon_{r,j+1} - \varepsilon_{r,j}) (1 - \frac{v^2}{c^2} \varepsilon_{r,j} + \frac{v}{c} \frac{k_{z,j+1}}{\omega/c})}{(1 - \frac{v^2}{c^2} \varepsilon_{r,j} + \frac{\kappa_1^2 v^2}{\omega^2}) (1 + \frac{v}{c} \frac{k_{z,j+1}}{\omega/c}) [\varepsilon_{r,j} \frac{k_{z,j+1}}{\omega/c} + \varepsilon_{r,j+1} \frac{k_{z,j}}{\omega/c}]} \quad (10)$$

$$a_{j|j+1}^{+,o} = \frac{\frac{v}{c} \frac{\kappa_1^2 c^2}{\omega^2 \varepsilon_{r,j+1}} (\varepsilon_{r,j+1} - \varepsilon_{r,j}) (1 - \frac{v^2}{c^2} \varepsilon_{r,j+1} - \frac{v}{c} \frac{k_{z,j}}{\omega/c})}{(1 - \frac{v^2}{c^2} \varepsilon_{r,j+1} + \frac{\kappa_1^2 v^2}{\omega^2}) (1 - \frac{v}{c} \frac{k_{z,j}}{\omega/c}) [\varepsilon_{r,j} \frac{k_{z,j+1}}{\omega/c} + \varepsilon_{r,j+1} \frac{k_{z,j}}{\omega/c}]} \quad (11)$$

The factors of $a_{j|j+1}^{-,o}$ in equation (10) and $a_{j|j+1}^{+,o}$ in equation (11) correspond to $a_{j|j+1}^-$ in equation (8) and $a_{j|j+1}^+$ in equation (9) for the case with $d_j = 0$, respectively.

The fields in equation (3), expressed in the Cartesian coordinates (x, y, z) , can also be transformed into the cylindrical coordinates (ρ, ϕ, z) . After some calculations, one has

$$\bar{E}_j(\bar{r}, t) = \bar{E}_j^q(\bar{r}, t) + \bar{E}_j^R(\bar{r}, t) \quad (12)$$

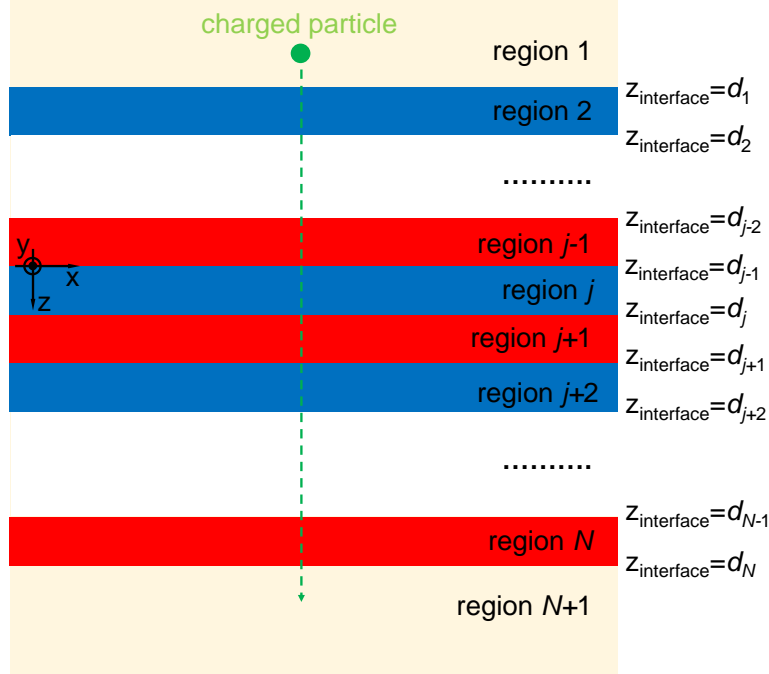
$$\begin{aligned} \bar{E}_j^q(\bar{r}, t) = \hat{z} \int_{-\infty}^{+\infty} d\omega \frac{-q}{8\pi\omega\varepsilon_0\varepsilon_{r,j}} \left(\frac{\omega^2}{c^2} \varepsilon_{r,j} - \frac{\omega^2}{v^2} \right) H_0^{(1)} \left(\rho \sqrt{\frac{\omega^2}{c^2} \varepsilon_{r,j} - \frac{\omega^2}{v^2}} \right) e^{i(\frac{\omega}{v}z - \omega t)} + \\ \hat{\rho} \int_{-\infty}^{+\infty} d\omega \frac{-q}{8\pi\omega\varepsilon_0\varepsilon_{r,j}} \left(i \frac{\omega}{v} \right) \left(-\sqrt{\frac{\omega^2}{c^2} \varepsilon_{r,j} - \frac{\omega^2}{v^2}} H_1^{(1)} \left(\rho \sqrt{\frac{\omega^2}{c^2} \varepsilon_{r,j} - \frac{\omega^2}{v^2}} \right) \right) e^{i(\frac{\omega}{v}z - \omega t)} \end{aligned} \quad (13)$$

$$\begin{aligned} \bar{E}_j^R(\bar{r}, t) = \hat{z} \int_{-\infty}^{+\infty} d\omega \int_0^{+\infty} d\kappa_\perp \cdot \frac{iq}{\omega\varepsilon_0(2\pi)^3} a_{j|j+1}^- \kappa_\perp (2\pi J_0(\kappa_\perp \rho)) e^{i[-k_{z,j}z - \omega t]} + \\ \hat{\rho} \int_{-\infty}^{+\infty} d\omega \int_0^{+\infty} d\kappa_\perp \cdot \frac{iq}{\omega\varepsilon_0(2\pi)^3} a_{j|j+1}^- k_{z,j} (i2\pi J_1(\kappa_\perp \rho)) e^{i[-k_{z,j}z - \omega t]} \end{aligned} \quad (14)$$

$$\bar{E}_{j+1}(\bar{r}, t) = \bar{E}_{j+1}^q(\bar{r}, t) + \bar{E}_{j+1}^R(\bar{r}, t) \quad (15)$$

$$\begin{aligned} \bar{E}_{j+1}^q(\bar{r}, t) = \hat{z} \int_{-\infty}^{+\infty} d\omega \frac{-q}{8\pi\omega\varepsilon_0\varepsilon_{r,j+1}} \left(\frac{\omega^2}{c^2} \varepsilon_{r,j+1} - \frac{\omega^2}{v^2} \right) H_0^{(1)} \left(\rho \sqrt{\frac{\omega^2}{c^2} \varepsilon_{r,j+1} - \frac{\omega^2}{v^2}} \right) e^{i(\frac{\omega}{v}z - \omega t)} + \\ \hat{\rho} \int_{-\infty}^{+\infty} d\omega \frac{-q}{8\pi\omega\varepsilon_0\varepsilon_{r,j+1}} \left(i \frac{\omega}{v} \right) \left(-\sqrt{\frac{\omega^2}{c^2} \varepsilon_{r,j+1} - \frac{\omega^2}{v^2}} H_1^{(1)} \left(\rho \sqrt{\frac{\omega^2}{c^2} \varepsilon_{r,j+1} - \frac{\omega^2}{v^2}} \right) \right) e^{i(\frac{\omega}{v}z - \omega t)} \end{aligned} \quad (16)$$

$$\begin{aligned} \bar{E}_{j+1}^R(\bar{r}, t) = \hat{z} \int_{-\infty}^{+\infty} d\omega \int_0^{+\infty} d\kappa_\perp \cdot \frac{iq}{\omega\varepsilon_0(2\pi)^3} a_{j|j+1}^+ \kappa_\perp (2\pi J_0(\kappa_\perp \rho)) e^{i[+k_{z,j+1}z - \omega t]} + \\ \hat{\rho} \int_{-\infty}^{+\infty} d\omega \int_0^{+\infty} d\kappa_\perp \cdot \frac{iq}{\omega\varepsilon_0(2\pi)^3} a_2(-k_{z,j+1}) (i2\pi J_1(\kappa_\perp \rho)) e^{i[+k_{z,j+1}z - \omega t]} \end{aligned} \quad (17)$$



Supplementary Fig. 2 | Structural schematic of resonance transition radiation when a charged particle perpendicularly crosses multiple interfaces.

Supplementary section 2: Resonance transition radiation from multiple interfaces

When a charged particle crosses a periodic structure, the presence of periodicity leads, naturally, to the coherent interference of emitted waves that appear at different interfaces, and as a consequence, to resonance effects [34, 35]. Therefore, transition radiation from a periodic structure is called the resonance transition radiation [37, 38, 51]. By extending Ginzburg and Frank’s theory on transition radiation to one-dimensional photonic crystals, we can analytically solve the resonance transition radiation when a charged particle perpendicularly crosses multiple interfaces; see Supplementary Fig. 2.

As a general analysis, we consider the studied system having $N + 1$ regions and N interfaces; see Supplementary Fig. 2. Region 1 and region $N + 1$ correspond to the top and bottom air regions, respectively. The rest of the setup is the same as that in supplementary note 1. Since the emitted fields of transition radiation at each interface can transmit into each region, the emitted fields in each region shall be a summation of transition radiation from each interface. Actually, transition radiation at each interface can be equivalently treated as the secondary radiation source, where its corresponding field distribution in the whole system is required to be solved. Below we demonstrate the main calculation procedure by separately solving the field distribution in each region from

the forward transition radiation at the $j - 1|j$ interface (i.e. the interface between region $j - 1$ and region j) and from the backward transition radiation at the $j|j + 1$ interface. The main procedure is similar to the calculation of the reflection/transmission in multilayer systems [52].

Part one: Field distribution in region j from the forward transition radiation at the $j - 1|j$ interface

For the forward transition radiation at the $j - 1|j$ interface, from equation (9), we have the forward radiation factor as follows:

$$a_{j-1|j}^+ = a_{j-1|j}^{+,o} e^{-ik_{z,j}d_{j-1}} e^{i\frac{\omega}{v}d_{j-1}} \quad (18)$$

From equation (7-2), the radiated field in region j becomes:

$$E_{z,j}^R = A_{j,o}^+ [e^{+ik_{z,j}(z-d_{j-1})} + \tilde{R}_{j|j+1} e^{-ik_{z,j}(z-d_{j-1})} \cdot e^{2ik_{z,j}(d_j-d_{j-1})}] \quad (19)$$

$$A_{j,o}^+ = \frac{iq}{\omega \varepsilon_0 (2\pi)^3} \cdot a_{j-1|j}^{+,o} e^{i\frac{\omega}{v}d_{j-1}} \cdot M_j \quad (20)$$

$$M_j = \frac{1}{1 - \tilde{R}_{j|j+1} \tilde{R}_{j|j-1} e^{2ik_{z,j}(d_j-d_{j-1})}} \quad (21)$$

In the above equations, the factor M_j characterizes the multiple reflections at the $j - 1|j$ and $j|j + 1$ interfaces; $\tilde{R}_{j|j+1}$ and $\tilde{R}_{j|j-1}$ are the *generalized reflection coefficients* of transverse-magnetic (TM, or p -polarized) waves for the multi-layer system at the $j|j + 1$ and $j|j - 1$ interfaces, respectively; see more introduction about the generalized reflection coefficient in Ref.[52]. In the subscript of $\tilde{R}_{j|j+1}$ and $\tilde{R}_{j|j-1}$, the TM plane wave is incident from region j (the first number) and transmitted to region $j + 1$ or $j - 1$ (the second number), respectively. This rule applies for other reflection and transmission coefficients of TM waves in the following. From Ref.[52], we have

$$\tilde{R}_{j|j+1} = R_{j|j+1} + \frac{T_{j|j+1} \tilde{R}_{j+1|j+2} T_{j+1|j} e^{2ik_{z,j+1}(d_{j+1}-d_j)}}{1 - R_{j+1|j} \tilde{R}_{j+1|j+2} e^{2ik_{z,j+1}(d_{j+1}-d_j)}} \quad (22-1)$$

$$\tilde{R}_{j|j-1} = R_{j|j-1} + \frac{T_{j|j-1} \tilde{R}_{j-1|j-2} T_{j-1|j} e^{2ik_{z,j-1}(d_{j-1}-d_{j-2})}}{1 - R_{j-1|j} \tilde{R}_{j-1|j-2} e^{2ik_{z,j-1}(d_{j-1}-d_{j-2})}} \quad (22-2)$$

where $\tilde{R}_{N|N+1} = R_{N|N+1}$ and $\tilde{R}_{2|1} = R_{2|1}$; $R_{j|j+1} = -R_{j+1|j} = \frac{k_{z,j} k_{z,j+1}}{\varepsilon_{r,j} \varepsilon_{r,j+1} + \frac{k_{z,j} k_{z,j+1}}{\varepsilon_{r,j} \varepsilon_{r,j+1}}}$ are the reflection coefficient; $T_{j|j+1} =$

$\frac{2 \frac{k_{z,j}}{\varepsilon_{r,j}} \cdot \frac{\varepsilon_{r,j}}{\varepsilon_{r,j+1}}}{\frac{k_{z,j} k_{z,j+1}}{\varepsilon_{r,j} \varepsilon_{r,j+1}} + \frac{k_{z,j} k_{z,j+1}}{\varepsilon_{r,j} \varepsilon_{r,j+1}}}$ and $T_{j+1|j} = \frac{2 \frac{k_{z,j+1}}{\varepsilon_{r,j+1}} \cdot \frac{\varepsilon_{r,j+1}}{\varepsilon_{r,j}}}{\frac{k_{z,j+1} k_{z,j}}{\varepsilon_{r,j+1} \varepsilon_{r,j}} + \frac{k_{z,j} k_{z,j+1}}{\varepsilon_{r,j} \varepsilon_{r,j+1}}}$ are the transmission coefficients. It is worthy to note that in this

work, the generalized reflection coefficients and other reflection/transmission coefficients are defined for the E_z field (see equation (19)), instead of the magnetic field. For TM waves, while the reflection coefficients for the E_z field and the magnetic field are the same (i.e. $R_{j|j+1}^{E_z} = R_{j|j+1}^H$), the transmission coefficients for the E_z field and the magnetic field are different (i.e. $T_{j|j+1}^{E_z} = T_{j|j+1}^H \cdot \frac{\varepsilon_{r,j}}{\varepsilon_{r,j+1}}$).

Part two: Field distribution in region m ($m > j$) from the forward transition radiation at the $j - 1|j$ interface

Since the forward transition radiation at the $j - 1|j$ interface propagates along the $+z$ direction, part of the emitted fields will transmit into region m ($m > j$). These transmitted fields in region m can be obtained by following the thought of calculating the reflection/transmission in multilayer systems [52]. The field in region m can be expressed as:

$$E_{z,m}^R = C_{j|m}^+ [e^{+ik_{z,m}(z-d_{j-1})} + \tilde{R}_{m|m+1} e^{-ik_{z,m}(z-d_{j-1})} \cdot e^{2ik_{z,m}(d_m-d_{j-1})}] \quad (23)$$

In equation (23), only the factor $C_{j|m}^+$ is unknown. When $m = j + 1$ in equation (23), at the $j|j + 1$ interface with $z = d_j$, we have

$$C_{j|j+1}^+ e^{+ik_{z,j+1}(d_j-d_{j-1})} = A_{j,o}^+ e^{+ik_{z,j}(d_j-d_{j-1})} \cdot S_{j|j+1} \quad (24)$$

$$S_{j|j+1} = \frac{T_{j|j+1}}{1 - R_{j+1|j} \tilde{R}_{j+1|j+2} e^{2ik_{z,j+1}(d_{j+1}-d_j)}} \quad (25)$$

Namely, the value of $C_{j|j+1}^+$ is determined by $A_{j,o}^+$ and the transmission at the $j|j + 1$ interface. By following the operation in equation (24), we have

$$C_{j|j+2}^+ e^{+ik_{z,j+2}(d_{j+1}-d_{j-1})} = C_{j|j+1}^+ e^{+ik_{z,j+1}(d_{j+1}-d_{j-1})} \cdot S_{j+1|j+2} \quad (26)$$

$$C_{j|j+3}^+ e^{+ik_{z,j+3}(d_{j+2}-d_{j-1})} = C_{j|j+2}^+ e^{+ik_{z,j+2}(d_{j+2}-d_{j-1})} \cdot S_{j+2|j+3} \quad (27)$$

.....

$$C_{j|m-1}^+ e^{+ik_{z,m-1}(d_{m-2}-d_{j-1})} = C_{j|m-2}^+ e^{+ik_{z,m-2}(d_{m-2}-d_{j-1})} \cdot S_{m-2|m-1} \quad (28)$$

$$C_{j|m}^+ e^{+ik_{z,m}(d_{m-1}-d_{j-1})} = C_{j|m-1}^+ e^{+ik_{z,m-1}(d_{m-1}-d_{j-1})} \cdot S_{m-1|m} \quad (29)$$

From equations (24-29), one has

$$C_{j|m}^+ e^{+ik_{z,m}(d_{m-1}-d_{j-1})} = \tilde{T}_{j|m}^{m>j} \cdot A_{j,o}^+ e^{+ik_{z,j}(d_{j-1}-d_{j-1})} \quad (30)$$

$$\tilde{T}_{j|m}^{m>j} = \prod_{n=j}^{m-1} S_{n|n+1} e^{+ik_{z,n}(d_n-d_{n-1})} \quad (31)$$

$\tilde{T}_{j|m}^{m>j}$ can be treated as the *generalized transmission coefficient* from region j to region m [52].

Part three: Field distribution in region m ($m < j$) from the forward transition radiation at the $j-1|j$ interface

Equation (19) can be equivalently transformed to following expression:

$$E_{z,j}^R = B_{j,o}^+ e^{+ik_{z,j}(z-d_{j-1})} + AR_{j,o}^- [e^{-ik_{z,j}(z-d_{j-1})} + \tilde{R}_{j|j-1} e^{+ik_{z,j}(z-d_{j-1})} e^{-2ik_{z,j}(d_{j-1}-d_{j-1})}] \quad (32)$$

$$AR_{j,o}^- = B_{j,o}^+ M_j \tilde{R}_{j|j+1} e^{2ik_{z,j}(d_j-d_{j-1})} \quad (33)$$

$$B_{j,o}^+ = \frac{A_{j,o}^+}{M_j} = \frac{iq}{\omega \varepsilon_0 (2\pi)^3} \cdot a_{j-1|j}^{+,o} e^{i\frac{\omega}{v} d_{j-1}} \quad (34)$$

In above transformation, the relation of $M_j = 1 + M_j \tilde{R}_{j|j+1} \tilde{R}_{j|j-1} e^{2ik_{z,j}(d_j-d_{j-1})}$ is used. When calculating the field distribution in transmitted region m ($m < j$) from the forward transition radiation at the $j-1|j$ interface, we only need to consider the second part relevant to $AR_{j,o}^-$ in equation (32). The calculation procedure is similar to that in *part two*. The field in region m ($m < j$) can be expressed as follows:

$$E_{z,m}^R = C_{j|m}^- [e^{-ik_{z,m}(z-d_{j-1})} + \tilde{R}_{m|m-1} e^{+ik_{z,m}(z-d_{j-1})} e^{-2ik_{z,m}(d_{m-1}-d_{j-1})}] \quad (35)$$

where only $C_{j|m}^-$ is unknown. When $m = j-1$ in equation (35), at the $j|j-1$ interface with $z = d_{j-1}$, we have

$$C_{j|j-1}^- e^{-ik_{z,j-1}(d_{j-1}-d_{j-1})} = AR_{j,o}^- e^{-ik_{z,j}(d_{j-1}-d_{j-1})} \cdot S_{j|j-1} \quad (36)$$

$$S_{j|j-1} = \frac{T_{j|j-1}}{1 - R_{j-1|j} \tilde{R}_{j-1|j-2} e^{2ik_{z,j-1}(d_{j-1}-d_{j-2})}} \quad (37)$$

By following the operation in equation (36), one has

$$C_{j|j-2}^- e^{-ik_{z,j-2}(d_{j-2}-d_{j-1})} = C_{j|j-1}^- e^{-ik_{z,j-1}(d_{j-2}-d_{j-1})} \cdot S_{j-1|j-2} \quad (38)$$

$$C_{j|j-3}^- e^{-ik_{z,j-3}(d_{j-3}-d_{j-1})} = C_{j|j-2}^- e^{-ik_{z,j-2}(d_{j-3}-d_{j-1})} \cdot S_{j-2|j-3} \quad (39)$$

.....

$$C_{j|m+1}^- e^{-ik_{z,m+1}(d_{m+1}-d_{j-1})} = C_{j|m+2}^- e^{-ik_{z,m+2}(d_{m+1}-d_{j-1})} \cdot S_{m+2|m+1} \quad (40)$$

$$C_{j|m}^- e^{-ik_{z,m}(d_m-d_{j-1})} = C_{j|m+1}^- e^{-ik_{z,m+1}(d_m-d_{j-1})} \cdot S_{m+1|m} \quad (41)$$

From equations (36-41), one has

$$C_{j|m}^- e^{-ik_{z,m}(d_m-d_{j-1})} = \tilde{T}_{j|m}^{m<j} \cdot AR_{j,o}^- e^{-ik_{z,j}(d_j-d_{j-1})} \quad (42)$$

$$\tilde{T}_{j|m}^{m<j} = \prod_{n=m}^{n=j-1} S_{n+1|n} e^{-ik_{z,n+1}(d_n-d_{n+1})} \quad (43)$$

$\tilde{T}_{j|m}^{m<j}$ is the *generalized transmission coefficient* from region j to region m [52]. The field distribution in region m ($m < j$) from the forward transition radiation at the $j-1|j$ interface can be solved by equation (42).

Part four: Field distribution in region j from the backward transition radiation at the $j|j+1$ interface

For the backward transition radiation at the $j|j+1$ interface, from equation (8), we have the backward radiation factor as:

$$a_{j|j+1}^- = a_{j|j+1}^{-,o} e^{+ik_{z,j}d_j} e^{i\frac{\omega}{v}d_j} \quad (44)$$

From equation (7-1), the emitted field in region j becomes:

$$E_{z,j}^R = A_{j,o}^- [e^{-ik_{z,j}(z-d_j)} + \tilde{R}_{j|j-1} e^{+ik_{z,j}(z-d_j)} \cdot e^{-2ik_{z,j}(d_{j-1}-d_j)}] \quad (45)$$

$$A_{j,o}^- = \frac{iq}{\omega\varepsilon_0(2\pi)^3} \cdot a_{j|j+1}^{-,o} e^{i\frac{\omega}{v}d_j} \cdot M_j \quad (46)$$

Equation (45) can be equivalently transformed to:

$$E_{z,j}^R = B_{j,o}^- e^{-ik_{z,j}(z-d_j)} + BR_{j,o}^+ [e^{+ik_{z,j}(z-d_j)} + \tilde{R}_{j|j+1} e^{-ik_{z,j}(z-d_j)} e^{+2ik_{z,j}(d_j-d_j)}] \quad (47)$$

$$BR_{j,o}^+ = B_{j,o}^- M_j \tilde{R}_{j|j-1} e^{-2ik_{z,j}(d_{j-1}-d_j)} \quad (48)$$

$$B_{j,o}^- = \frac{A_{j,o}^-}{M_j} = \frac{iq}{\omega\varepsilon_0(2\pi)^3} \cdot a_{j|j+1}^{-,o} e^{i\frac{\omega}{v}d_j} \quad (49)$$

Part five: Field distribution in region m ($m > j$) from the backward transition radiation at the $j|j+1$ interface

By using the second part relevant to $BR_{j,o}^+$ in equation (47), the field distribution in region m ($m > j$) from the backward transition radiation at the $j|j+1$ interface can be obtained. The field in region m can be expressed as:

$$E_{z,m}^R = D_{j|m}^+ [e^{+ik_{z,m}(z-d_j)} + \tilde{R}_{m|m+1} e^{-ik_{z,m}(z-d_j)} \cdot e^{2ik_{z,m}(d_m-d_j)}] \quad (50)$$

The calculation procedure for the unknown factor $D_{j|m}^+$ is the same as that of $C_{j|m}^+$ in *part two*. After some algebra, we have

$$D_{j|m}^+ e^{+ik_{z,m}(d_{m-1}-d_j)} = \tilde{T}_{j|m}^{m>j} \cdot BR_{j,o}^+ e^{+ik_{z,j}(d_{j-1}-d_j)} \quad (51)$$

Part six: Field distribution in region m ($m < j$) from the backward transition radiation at the $j|j + 1$ interface

By using equation (45), the field distribution in transmitted region m ($m < j$) from the backward transition radiation at the $j|j + 1$ interface can be obtained. The field in region m ($m < j$) can be expressed as:

$$E_{z,m}^R = D_{j|m}^- [e^{-ik_{z,m}(z-d_j)} + \tilde{R}_{m|m-1} e^{+ik_{z,m}(z-d_j)} e^{-2ik_{z,m}(d_{m-1}-d_j)}] \quad (52)$$

The calculation procedure for the unknown factor $D_{j|m}^-$ is the same as that of C_m^- in *part three*. After some algebra, we have

$$D_{j|m}^- e^{-ik_{z,m}(d_m-d_j)} = \tilde{T}_{j|m}^{m < j} \cdot A_{j,o}^- e^{-ik_{z,j}(d_j-d_j)} \quad (53)$$

This way, the field distribution in region m ($m < j$) from the backward transition radiation at the $j|j + 1$ interface can be obtained by using equation (53).

Part seven: Field distribution in region j from resonance transition radiation at multiple interfaces

From above analysis, the total radiated field in region j ($1 \leq j \leq N + 1$) can be a summation of two parts, i.e.

$$E_{z,j}^R = E_{z,j}^{R,+} + E_{z,j}^{R,-} \quad (54)$$

where $E_{z,j}^{R,+}$ and $E_{z,j}^{R,-}$ are attributed to the forward and backward transition radiations at each interface, respectively. Namely, $E_{z,j}^{R,+}$ is a summation of the emitted fields from the forward transition radiation at each interface transmitted into region j , and $E_{z,j}^{R,-}$ is a summation of the emitted fields from the backward transition radiation at each interface transmitted into region j . Therefore, we have

$$E_{z,j}^{R,+} = TR_j^+ \rightarrow Region_j + \sum_{m=1}^{m=j-1} TR_m^+ \rightarrow Region_j + \sum_{m=j+1}^{m=N+1} TR_m^+ \rightarrow Region_j \quad (55)$$

$$TR_j^+ \rightarrow Region_j = A_{j,o}^+ [e^{+ik_{z,j}(z-d_{j-1})} + \tilde{R}_{j|j+1} e^{-ik_{z,j}(z-d_{j-1})} \cdot e^{2ik_{z,j}(d_j-d_{j-1})}] \quad (56)$$

$$\sum_{m=1}^{m=j-1} TR_m^+ \rightarrow Region_j = \sum_{m=1}^{m=j-1} C_{m|j}^+ [e^{+ik_{z,j}(z-d_{m-1})} + \tilde{R}_{j|j+1} e^{-ik_{z,j}(z-d_{m-1})} \cdot e^{2ik_{z,j}(d_j-d_{m-1})}] \quad (57)$$

$$\sum_{m=j+1}^{m=N+1} TR_m^+ \rightarrow Region_j = \sum_{m=j+1}^{m=N+1} C_{m|j}^- [e^{-ik_{z,j}(z-d_{m-1})} + \tilde{R}_{j|j-1} e^{+ik_{z,j}(z-d_{m-1})} e^{-2ik_{z,j}(d_{j-1}-d_{m-1})}] \quad (58)$$

$$E_{z,j}^{R,-} = TR_j^- \rightarrow Region_j + \sum_{m=1}^{m=j-1} TR_m^- \rightarrow Region_j + \sum_{m=j+1}^{m=N+1} TR_m^- \rightarrow Region_j \quad (59)$$

$$TR_j^- \rightarrow Region_j = A_{j,o}^- [e^{-ik_{z,j}(z-d_j)} + \tilde{R}_{j|j-1} e^{+ik_{z,j}(z-d_j)} \cdot e^{-2ik_{z,j}(d_{j-1}-d_j)}] \quad (60)$$

$$\sum_{m=1}^{m=j-1} TR_m^- \rightarrow Region_j = \sum_{m=1}^{m=j-1} D_{m|j}^+ [e^{+ik_{z,j}(z-d_m)} + \tilde{R}_{j|j+1} e^{-ik_{z,j}(z-d_m)} \cdot e^{2ik_{z,j}(d_j-d_m)}] \quad (61)$$

$$\sum_{m=j+1}^{m=N+1} TR_m^- \rightarrow Region_j = \sum_{m=j+1}^{m=N+1} D_{m|j}^- [e^{-ik_{z,j}(z-d_m)} + \tilde{R}_{j|j-1} e^{+ik_{z,j}(z-d_m)} e^{-2ik_{z,j}(d_{j-1}-d_m)}] \quad (62)$$

This way, we can obtain the field distribution of resonance transition radiation from multiple interfaces in each region by using equations (55-62). For regions $j = 1$ and $j = N + 1$, the radiated fields only propagate along the $-z$ and $+z$ directions, respectively. When $j = 1$, we have

$$E_{z,1}^{R,-} = \frac{iq}{\omega\varepsilon_0(2\pi)^3} \cdot a_1 \cdot e^{-ik_{z,1}z} \quad (63)$$

$$a_1 = \frac{\omega\varepsilon_0(2\pi)^3}{iq} (A_{1,0}^- e^{+ik_{z,1}d_j} + \sum_{m=2}^{m=N+1} D_{m|1}^- e^{+ik_{z,1}d_m} + \sum_{m=2}^{m=N+1} C_{m|1}^- e^{+ik_{z,1}d_{m-1}}) \quad (64)$$

When $j = N + 1$, we have

$$E_{z,N+1}^{R,+} = \frac{iq}{\omega\varepsilon_0(2\pi)^3} \cdot a_{N+1} \cdot e^{+ik_{z,N+1}z} \quad (65)$$

$$a_{N+1} = \frac{\omega\varepsilon_0(2\pi)^3}{iq} (A_{N+1,0}^+ e^{-ik_{z,N+1}d_N} + \sum_{m=1}^{m=N} C_{m|N+1}^+ e^{-ik_{z,N+1}d_{m-1}} + \sum_{m=1}^{m=N} D_{m|N+1}^+ e^{-ik_{z,N+1}d_m}) \quad (66)$$

It is worthy to note that the form of equations (63,65) is the same as that of equations (7-1,7-2).

Supplementary section 3: Angular spectral energy density of resonance transition radiation

The angular spectral energy density of resonance transition radiation in the forward and backward directions can be analytically obtained, with the calculation procedure briefly introduced below; see more details in our previous work [38]. One can obtain the total energy W_1 radiated by a charged particle into region 1 (top air region), i.e. backwards relative to its motion, by integrating the emitted field energy density over all space. For a long time t , the radiated wave-train is already at a great distance to the interface and then separated from the charge's intrinsic field. If the origin is moved along the axis into the region of the radiated wave-train, the integration with respect to z can be taken from $-\infty$ to $+\infty$, since the field is attenuated in both directions [38].

For freely propagating waves, since the electric and magnetic energy densities are equal, one has

$$W_1 = \int dx dy \int_{-\infty}^{+\infty} dz \cdot \varepsilon_1 |\bar{E}_1^R(\vec{r}, t)|^2 \quad (67)$$

$$|\bar{E}_1^R(\vec{r}, t)|^2 = \int \bar{E}_{1|\bar{\kappa}_\perp, \omega}^R(z) \cdot \bar{E}_{1|\bar{\kappa}'_\perp, \omega'}^{R*}(z) e^{i[(\bar{\kappa}_\perp - \bar{\kappa}'_\perp) \cdot \vec{r}_\perp - (\omega - \omega')t]} d\bar{\kappa}_\perp d\bar{\kappa}'_\perp d\omega d\omega' \quad (68)$$

Substituting equation (68) into equation (67) and integrating over $dx dy d\bar{\kappa}'_\perp dz d\omega'$ in equation (67) gives

$$W_1 = 2 \int_0^{+\infty} \int \varepsilon_1 |a_1|^2 \left(\frac{q}{\omega\varepsilon_0(2\pi)^3} \right)^2 \frac{\omega^2}{c\kappa_\perp^2} \sqrt{\varepsilon_{1r}} \sqrt{1 - \frac{\kappa_\perp^2 c^2}{\omega^2 \varepsilon_{1r}}} (2\pi)^3 d\bar{\kappa}_\perp d\omega \quad (69)$$

For emitted photons, the integration over $d\bar{\kappa}_\perp$ is to be taken over the range $\kappa_\perp^2 < \frac{\omega^2}{c^2} \varepsilon_{1r}$. We use the angle θ between the radiation wave vector $\bar{k}_1 = (\bar{\kappa}_\perp, \hat{z}k_{1z})$ and the direction of the vector $-\bar{v}$, so that $\theta = 0$ represents radiation in the opposite direction of the particle's motion. Then we can express $\kappa_\perp = \frac{\omega}{c} \sqrt{\varepsilon_{1r}} \sin\theta$. A further change from integration over $d\bar{\kappa}_\perp$ to one over $2\pi\kappa_\perp d\kappa_\perp = 2\pi(\frac{\omega^2}{c^2} \varepsilon_{1r}) \sin\theta \cos\theta d\theta$ in equation (69) gives

$$W_1 = \int_0^{+\infty} \int_0^{\pi/2} U_1(\omega, \theta) \cdot (2\pi \sin\theta) d\theta d\omega \quad (70)$$

$$U_1(\omega, \theta) = \frac{\varepsilon_{1r}^{3/2} q^2 \cos^2 \theta}{4\pi^3 \varepsilon_0 c \sin^2 \theta} |a_1|^2 \quad (71)$$

Equation (71) is the backward angular spectral energy density, which shows the distribution of the radiation as a function of frequency and angle. With equation (64), the backward angular spectral energy density in equation (71) can be obtained straightforwardly. By expressing the total energy as $W_1 = \int_0^\infty W_1(\omega) d\omega$, one has the energy spectrum of resonance transition radiation in the backward direction as

$$W_1(\omega) = \int_0^{\pi/2} U_1(\omega, \theta) \cdot (2\pi \sin\theta) d\theta \quad (72)$$

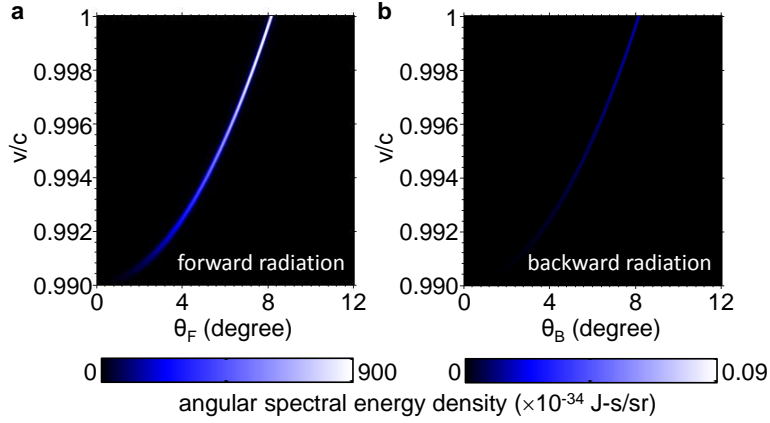
By following the calculation procedure above, the forward angular spectral energy density and the energy spectrum of resonance transition radiation in region $N + 1$ (bottom air region) can also be obtained as:

$$U_{N+1}(\omega, \theta) = \frac{\varepsilon_{r,N+1}^{3/2} q^2 \cos^2 \theta}{4\pi^3 \varepsilon_0 c \sin^2 \theta} |a_{N+1}|^2 \quad (73)$$

$$W_{N+1}(\omega) = \int_0^{\pi/2} U_{N+1}(\omega, \theta) \cdot (2\pi \sin\theta) d\theta \quad (74)$$

With equation (66), the forward angular spectral energy density in equation (73) can be calculated straightforwardly. Note that the definitions of the radiation angle for the backward radiation in equations (71) and the forward radiation in equation (73) are different. For the backward radiation in equations (71), the radiation angle as stated above is the angle between the radiation wave vector $\bar{k}_1 = (\bar{\kappa}_\perp, \hat{z}k_{1z})$ and the vector $-\bar{v}$; namely $\theta = \theta_B$ in Fig. 1. For the forward radiation in equations (73), the radiation angle is the angle between the radiation wave vector $\bar{k}_1 = (\bar{\kappa}_\perp, \hat{z}k_{1z})$ and the vector $+\bar{v}$; namely $\theta = \theta_F$ in Fig. 1.

The total emitted photon spectrum is $W(\omega) = W_1(\omega) + W_2(\omega)$. The total energy of emitted photons into the top and bottom air regions can be obtained by integrating over frequency.



Supplementary Fig. 3 | Cherenkov radiation from an isotropic slab. The isotropic slab with a refractive index of $n = 1.01$ has a thickness of 2 mm. The structure is air-dielectric slab-air. **a,b**, Angular spectral energy density of forward (backward) radiation in the bottom (top) air region at the working frequency (corresponding wavelength in air is $\lambda = 700$ nm).

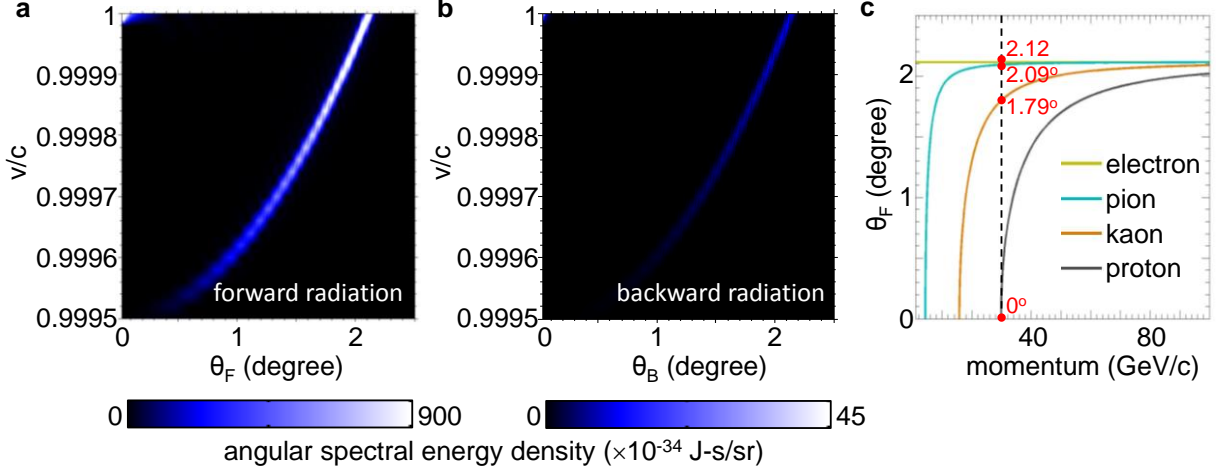
Angular spectral energy density of transition radiation from an isotropic slab

Supplementary Figure 3 shows the angular spectral energy density of transition radiation from an isotropic slab with a hypothetical refractive index of $n = 1.01$. The highly directional radiation in Supplementary Fig. 3a shows the relation between the Cherenkov angle and the particle velocity (denoted as the Cherenkov relation below). From the Cherenkov relation, the isotropic slab will have the forward Cherenkov radiation when the particle velocity is in the range of $[0.99c]$. The corresponding range for the Cherenkov angle in the air region is $[0.8, 1.1]$ degree. The angular spectral energy density in the forward direction in Supplementary Fig. 3a is $\sim 10^5$ times of that in the backward direction in Supplementary Fig. 3b.

Forward Cherenkov relation of photonic crystals for particle identification with other velocity or momentum

Here we demonstrate the forward Cherenkov relation from an alternative photonic crystal that can enable the identification of particles with the extremely high velocity or momentum, as shown in Supplementary Fig. 4. The highly directional radiation in Supplementary Fig. 4a,b shows the Cherenkov relation of the photonic crystal. The corresponding ranges of the particle velocity and the Cherenkov angle in the air region are $[0.9995c, c]$ and $[0.2, 1.1]$ degree, respectively. The angular spectral energy density in the forward direction in Supplementary Fig. 4a is ~ 100 times larger than that in the backward direction in Supplementary Fig. 4b. Therefore, the resonance transition radiation from the photonic crystal here is equivalent to the forward Cherenkov radiation. By applying the Cherenkov relation in Supplementary Fig. 4a, Supplementary Fig. 4c shows the relation between the particle

momentum and the Cherenkov angle for four kinds of particles with different masses. For different particles with the same momentum being as high as 29.7 GeV/c, the corresponding Cherenkov angle is 2.12°, 2.09°, 1.79°, and 0° for the electron, pion, kaon, and proton, respectively. These Cherenkov angles are different enough to enable effectively distinguishing between the different particles.



Supplementary Fig. 4 | Controlling the forward Cherenkov angle by photonic crystals. For the studied photonic crystal, the thickness of the unit cell is $d_{unit} = 1.0146\lambda$; within the unit cell, the thicknesses for the two dielectric constituents are $d_1 = 0.3d_{unit}$ and $d_2 = 0.7d_{unit}$, respectively. The total thickness of the photonic crystal is 50 mm. **a,b**, Angular spectral energy density of forward (backward) radiation in the bottom (top) air region. **c**, Cherenkov angles versus the particle momentum for four kinds of particles. These results adopt the relation between the particle velocity and the Cherenkov angle in **a**, and translate the velocity to the momentum using the masses of different charged particles.

Supplementary section 4: Resonance transition radiation from a uniaxial system

The calculation procedure of resonance transition radiation in a uniaxial system is similar to that in supplementary notes 1-3, which is briefly summarized below. We only consider resonance transition radiation in an isotropic system in supplementary notes 1-3, where all regions are composed of isotropic materials. Actually, resonance transition radiation from multiple interfaces can also be analytically solved when the material in each becomes uniaxial with the relative permittivity being $\bar{\bar{\epsilon}}_{r,j} = [\epsilon_{r,\perp,j}, \epsilon_{r,\perp,j}, \epsilon_{r,z,j}]$ for region j [34, 35]. When $\epsilon_{r,\perp,j} = \epsilon_{r,z,j} = \epsilon_{r,j}$, the material in region j becomes isotropic again.

For transition radiation from a single interface, when the two regions becomes uniaxial, the freely radiated fields can be still be expressed by equations (7-9), but the two radiation facts of $\bar{a}_{j|j+1}^{-,o}$ in equation (10) and $\bar{a}_{j|j+1}^{+,o}$ in equation (10) are changed to:

$$a_{j|j+1}^{-,o} = \frac{\kappa_{\perp}^2 c^2}{\omega^2} \cdot \frac{-v}{c} \cdot \frac{\varepsilon_{r,\perp,j} \varepsilon_{r,\perp,j+1}}{\varepsilon_{r,z,j}} \cdot \frac{\frac{1 - \frac{v}{c} \frac{k_{z,j+1}}{\omega/c}}{\varepsilon_{r,z,j+1} (1 - \frac{v^2}{c^2} \varepsilon_{r,\perp,j+1} + \frac{\kappa_{\perp}^2 v^2 \varepsilon_{r,\perp,j+1}}{\omega^2 \varepsilon_{r,z,j+1}})} - \frac{1 - \frac{v}{c} \frac{k_{z,j+1}}{\omega/c} \frac{\varepsilon_{r,\perp,j}}{\varepsilon_{r,\perp,j+1}}}{\varepsilon_{r,z,j} (1 - \frac{v^2}{c^2} \varepsilon_{r,\perp,j} + \frac{\kappa_{\perp}^2 v^2 \varepsilon_{r,\perp,j}}{\omega^2 \varepsilon_{r,z,j}})}}{\varepsilon_{r,\perp,j} \frac{k_{z,j+1}}{\omega/c} + \varepsilon_{r,\perp,j+1} \frac{k_{z,j}}{\omega/c}} \quad (75)$$

$$a_{j|j+1}^{+,o} = \frac{\kappa_{\perp}^2 c^2}{\omega^2} \cdot \frac{+v}{c} \cdot \frac{\varepsilon_{r,\perp,j} \varepsilon_{r,\perp,j+1}}{\varepsilon_{r,z,j+1}} \cdot \frac{\frac{1 + \frac{v}{c} \frac{k_{z,j}}{\omega/c}}{\varepsilon_{r,z,j} (1 - \frac{v^2}{c^2} \varepsilon_{r,\perp,j} + \frac{\kappa_{\perp}^2 v^2 \varepsilon_{r,\perp,j}}{\omega^2 \varepsilon_{r,z,j}})} - \frac{1 + \frac{v}{c} \frac{k_{z,j}}{\omega/c} \frac{\varepsilon_{r,\perp,j+1}}{\varepsilon_{r,\perp,j}}}{\varepsilon_{r,z,j+1} (1 - \frac{v^2}{c^2} \varepsilon_{r,\perp,j+1} + \frac{\kappa_{\perp}^2 v^2 \varepsilon_{r,\perp,j+1}}{\omega^2 \varepsilon_{r,z,j+1}})}}{\varepsilon_{r,\perp,j} \frac{k_{z,j+1}}{\omega/c} + \varepsilon_{r,\perp,j+1} \frac{k_{z,j}}{\omega/c}} \quad (76)$$

In addition, it is worthy to note that the component of the wavevectors for the radiated fields along the z direction

are changed to $k_{z,j} = \sqrt{\frac{\varepsilon_{r,\perp,j} \omega^2}{c^2} - \kappa_{\perp}^2 \frac{\varepsilon_{r,\perp,j}}{\varepsilon_{r,z,j}}}$ and $k_{z,j+1} = \sqrt{\frac{\varepsilon_{r,\perp,j+1} \omega^2}{c^2} - \kappa_{\perp}^2 \frac{\varepsilon_{r,\perp,j+1}}{\varepsilon_{r,z,j+1}}}$, respectively.

For resonance transition radiation from multiple interfaces in a uniaxial system, the field distribution in each region can still be expressed by equations (54-66). However, the reflection and transmission coefficients at each

interface (see the text below equation (22-2)) are changed to $R_{j|j+1} = -R_{j+1|j} = \frac{\frac{k_{z,j}}{\varepsilon_{r,\perp,j}} - \frac{k_{z,j+1}}{\varepsilon_{r,\perp,j+1}}}{\frac{k_{z,j}}{\varepsilon_{r,\perp,j}} + \frac{k_{z,j+1}}{\varepsilon_{r,\perp,j+1}}}$, $T_{j|j+1} =$

$$\frac{2 \frac{k_{z,j}}{\varepsilon_{r,\perp,j}}}{\frac{k_{z,j}}{\varepsilon_{r,\perp,j}} + \frac{k_{z,j+1}}{\varepsilon_{r,\perp,j+1}}} \cdot \frac{\varepsilon_{r,z,j}}{\varepsilon_{r,z,j+1}} \text{ and } T_{j+1|j} = \frac{2 \frac{k_{z,j+1}}{\varepsilon_{r,\perp,j+1}}}{\frac{k_{z,j+1}}{\varepsilon_{r,\perp,j+1}} + \frac{k_{z,j}}{\varepsilon_{r,\perp,j}}} \cdot \frac{\varepsilon_{r,z,j+1}}{\varepsilon_{r,z,j}}, \text{ respectively.}$$

Since we consider the top and bottom regions both to be the isotropic air region in this work, the backward and forward angular spectral energy densities of resonance transition radiation in a uniaxial system can still be expressed by equations (71,73), respectively.

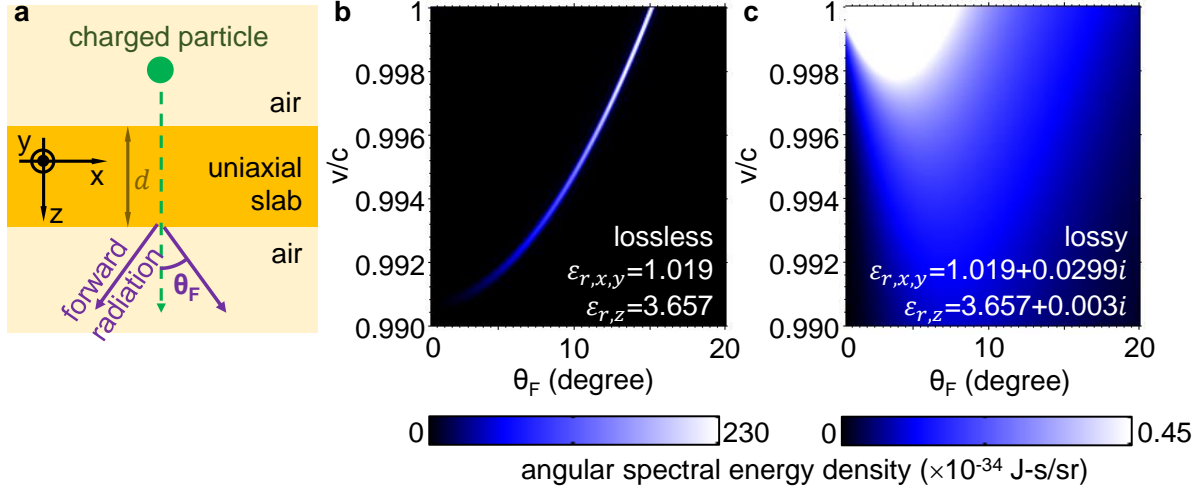
Loss influence on the angular spectral energy density of transition radiation from a uniaxial slab

Recently, uniaxial metal-based metamaterials were proposed for the control of the Cherenkov relation in Cherenkov detectors [14]. Since losses are unavoidable in the metal-based systems, Supplementary Fig. 5 investigate the loss influence on the angular spectral energy density of the forward Cherenkov radiation from a uniaxial slab; see the structure in Supplementary Fig. 5a. For brevity, we consider the permittivity of the uniaxial slab to be equal to the permittivity of the uniaxial metal-based metamaterials used in this recent paper (Ref. [14]).

When the loss is neglected, the Cherenkov relation can be clearly seen from the forward angular spectral energy density in Supplementary Fig. 5b. However, when the realistic loss is considered, the Cherenkov relation is severely distorted (e.g., broadened) and may even be practically destroyed, as shown in Supplementary Fig. 5c.

In addition, the value of the forward angular spectral energy density for the lossless case in Supplementary Fig.

5b is over 200 times larger than that for the lossy case in Supplementary Fig. 5c. Therefore, the realistic loss is detrimental to the performance of Cherenkov detectors, and it shall be judicious to control the Cherenkov relation in lossless systems.



Supplementary Fig. 5 | Loss influence on the forward Cherenkov radiation from a uniaxial slab. **a**, Structural schematic. The uniaxial slab with a thickness of $d = 2$ mm has a relative permittivity of $[\epsilon_{r,x}, \epsilon_{r,y}, \epsilon_{r,z}]$, where $\epsilon_{r,x} = \epsilon_{r,y}$. **b,c**, Angular spectral energy density of the forward radiation in the top air region from a **(b)** lossless and **(c)** lossy uniaxial slab. For the lossy case in **c**, the relative uniaxial permittivity, which is adopted from Ref. [14], stands for a metal-based uniaxial metamaterials. For the ideal lossless case in **b**, the imaginary part of the uniaxial permittivity is neglected.

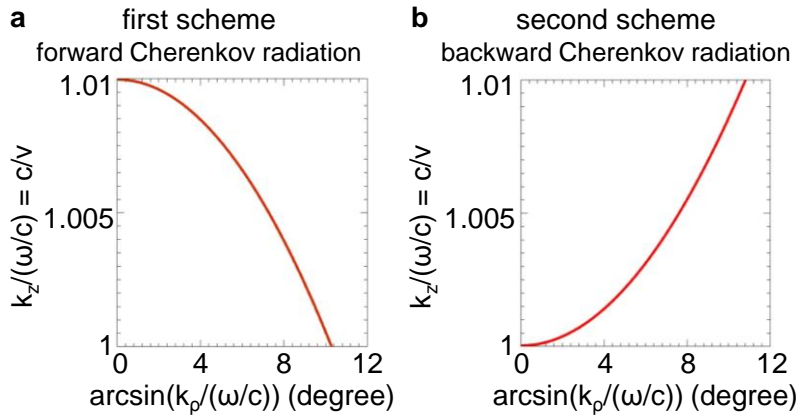
Supplementary section 5: Band structure and isofrequency contour of one-dimensional photonic crystals

The dispersion of 1D photonic crystal has been extensively studied and can be calculated by matching the boundary condition with the help of Bloch's theorem (or Bloch-periodic boundary condition) [30]. In this work, the 1D photonic crystal is composed by two different isotropic materials along the z direction, where their relative permittivities are $\epsilon_{r,1}$ and $\epsilon_{r,2}$, respectively. For a periodic unit cell with a total thickness of $d = d_1 + d_2$, the thickness of these two materials are d_1 and d_2 , respectively. The dispersion of the 1D photonic crystal for TM waves can be expressed as:

$$\cos(k_z d) = \cos(k_{z1} d_1) \cos(k_{z2} d_2) - \frac{1}{2} \left(\frac{Y_1}{Y_2} + \frac{Y_2}{Y_1} \right) \sin(k_{z1} d_1) \sin(k_{z2} d_2) \quad (77)$$

$$Y_1 = \omega \epsilon_0 \epsilon_{r,1} / k_{z1}; Y_2 = \omega \epsilon_0 \epsilon_{r,2} / k_{z2} \quad (78)$$

In above equations, $k_{z,1} = \sqrt{\frac{\epsilon_{r,1}\omega^2}{c^2} - \kappa_{\perp}^2}$ and $k_{z,2} = \sqrt{\frac{\epsilon_{r,2}\omega^2}{c^2} - \kappa_{\perp}^2}$; κ_{\perp} , same as that in supplementary notes 1-4, is the magnitude of the component of the wavevector parallel to the interface. When $\kappa_{\perp} = 0$, equation (77) characterizes the relation between the angular frequency ω and the component of the wavevector along the z direction (i.e. k_z). By solving the case of $\kappa_{\perp} = 0$, the band structure for the 1D photonic crystal can be obtained. When the angular frequency is a constant with $\omega = \omega_0$, equation (77) characterizes the relation between k_z and κ_{\perp} . By solving the case of $\omega = \omega_0$, the isofrequency contour of the 1D photonic crystal at $\omega = \omega_0$ can be obtained; see Supplementary Fig. 6 for example.

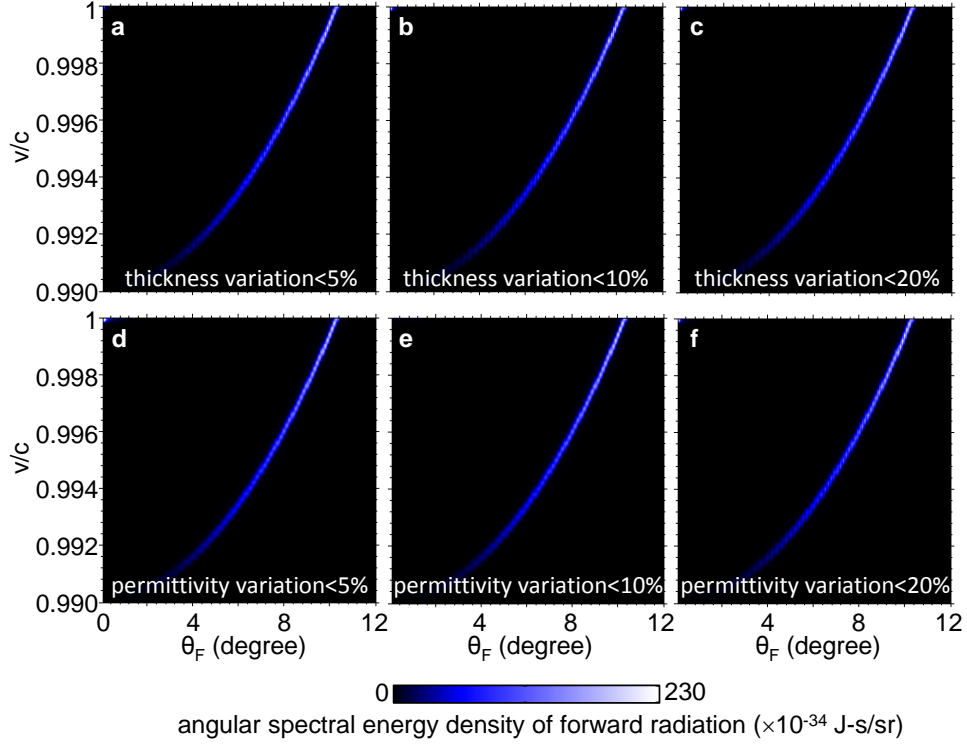


Supplementary Fig. 6 | Isofrequency contours of photonic crystal (a) in Fig. 3a and (b) in Fig. 4. These two isofrequency contours are designed for the generation of forward and backward Cherenkov radiation, respectively. The working wavelength is 700 nm.

Supplementary section 6: Various features of Cherenkov radiation from photonic crystals

(6.1) Impact of local disorders on Cherenkov radiation from photonic crystals

The impacts from the local disorders in photonic crystals on the performance of Cherenkov radiation are discussed in Supplementary Fig. 7. The local disorder is exemplified by assuming that there is a uniformly-distributed random change of the thickness (i.e., structural variation) or the permittivity (i.e., material variation) for a certain number of periods of photonic crystal in Fig. 3a. Supplementary Figure 7 indicates that Cherenkov radiation from photonic crystal is insensitive to these local disorders.



Supplementary Fig. 7 | Impact of local disorders, including (a-c) structural variation and (d-f) material variation, on the angular spectral energy density of forward radiation from photonic crystals. When there is no disorder, the photonic crystal is the same as that in Fig. 3a, where its total number of periods is 2800. When there is local disorder, it is assumed that there is a uniformly-distributed random change in the thickness (i.e., structural variation) or the permittivity (i.e., material variation) for the first 50 periods in the photonic crystal. The maximum relative change in each parameter is 5% in **a,d**, 10% in **b,e**, and 20% in **c,f**, respectively. A similar change in different layers yield similar results.

(6.2) Angular spread of Cherenkov radiation from photonic crystals

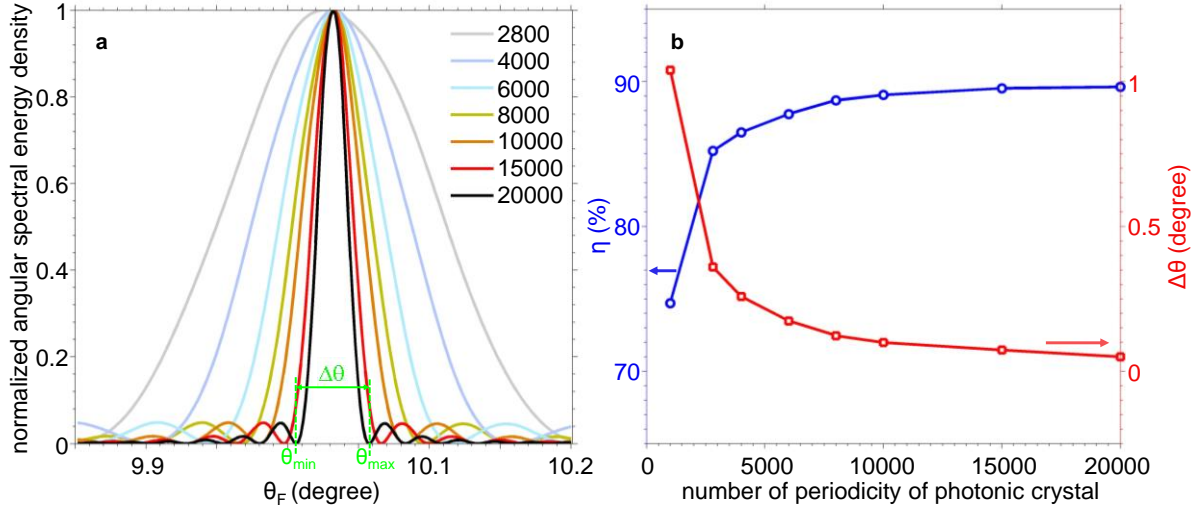
Supplementary Figure 8a shows the angular spectral energy density of forward radiation $U_{N+1}(\omega_0, \theta)$ for different thicknesses of photonic crystal at a fixed frequency and at a fixed particle velocity. Here we explore the angular spread of the radiation within the main lobe of $U_{N+1}(\omega_0, \theta)$. The main lobe has an angular spread of $\Delta\theta = \theta_{max} - \theta_{min}$. This way, the fraction of Cherenkov radiation radiated into the main lobe is defined as $\eta =$

$$\frac{\int_{\theta_{min}}^{\theta_{max}} U_{N+1}(\omega_0, \theta) d\theta}{\int_0^{\pi/2} U_{N+1}(\omega_0, \theta) d\theta}. \text{ Supplementary Figure 8b shows the values of } \eta \text{ and } \Delta\theta \text{ under different number of periods}$$

for photonic crystals. When the number of periods increases, η increases to $\sim 90\%$ and the angular spread $\Delta\theta$ decreases (down to less than 0.05°). We find the same behavior for different wavelengths and particle velocities.

For the photonic crystal in Fig. 3a, $\eta = 85\%$ and $\Delta\theta = 0.36^\circ$ when $v = 0.9995c$.

Since the relation between Cherenkov angle and particle velocity (or momentum) is directly extracted from the angular spectral energy density, there will be an uncertainty contributed by the angular spread of Cherenkov radiation. This may come from the finite thickness of photonic crystal as can be inferred from Supplementary Fig. 8. Therefore, one way to improve the precision in measurement for high particle momentum is to adopt a sufficiently thick photonic crystal.



Supplementary Fig. 8 | Angular spread of forward Cherenkov radiation from a photonic crystal. **a**, Normalized angular spectral energy density of forward radiation, i.e., $U_{N+1}(\omega_0, \theta)/\max(U_{N+1}(\omega_0, \theta))$. Here $N = 2M + 1$, where M is the number of periods in the photonic crystal. The values of M are denoted in the legend. For this example, the wavelength is $\lambda_0 = 700$ nm, $\omega_0 = 2\pi c/\lambda_0$, and the particle velocity is $v = 0.9995c$. The photonic crystal's layers are the same as that in Fig. 3a. **b**, Angular spread of Cherenkov radiation $\Delta\theta$, and the fraction η of energy radiated into the angle range of $[\theta_{min}, \theta_{max}]$ versus the number of periods. θ_{min} and θ_{max} , as denoted in **a**, are the angles on the two sides of the main lobe where $U_{N+1}(\omega_0, \theta)$ reaches local minima (dips).

(6.3) Momentum range for particle identification

There is a trade-off between the ability to measure particles of relatively high mass (e.g., proton) and to separate between particles of low mass (e.g., electron and pion). To cover a wider momentum range, one can use multiple photonic crystal radiators, each designed to cover a different range. This is elaborated below.

As the momentum of the charged particle increases, the plots of “Cherenkov angle vs momentum” for different particle types are expected to converge, regardless of whether it is in a conventional dielectric medium or in a photonic crystal. This can be seen from the standard formula for Cherenkov radiation in a dielectric medium.

When a charged particle with a rest mass m and momentum p moves with a velocity $v = \beta c$ in a dielectric with

refractive index n , the Cherenkov angle θ is given by $\cos\theta = \frac{1}{n\beta}$. Here, $\beta = \frac{p}{\sqrt{p^2+m^2c^2}} = \frac{1}{\sqrt{1+m^2c^2/p^2}}$. (SI units used here, and c is the speed of light in vacuum). From this, one can infer that as the particle momentum increases to large values, $\beta \rightarrow 1$ and $\theta \rightarrow \cos^{-1}(1/n)$. Hence, the Cherenkov angle becomes independent of the particle type. As the particle momentum decreases, the curves for different particle types separate out until they vanish at the corresponding Cherenkov thresholds, i.e., where $\theta = 0$, $\beta = 1/n$ and $p = mc(n^2 - 1)^{-1/2}$. This also means that a smaller refractive index or effective refractive index is needed to maintain the angular detection sensitivity at high momentum.

An example of this dependence on refractive index and momentum in real data can be seen in Fig. 14 of Ref. [11]. Indeed during the design of Cherenkov detectors, the choice of radiator depends on the momentum range and particle type that is envisaged for particle identification. To cover a large momentum range, multiple radiators each with a different refractive index are needed. As an example, to cover a momentum range of 2-100 GeV/c, three different radiators were used in Ref. [53] as indicated in Fig. 6.1 there.

The same behavior is expected in the case of the effective Cherenkov radiation from the photonic crystals we designed, as indicated in Fig. 3 and Fig. 4 of our manuscript. In particular, a photonic crystal can be designed to have high sensitivity for electron-pion separation in a certain momentum range at the cost of being potentially below threshold and thus insensitive to protons in the same momentum range. As with conventional radiators, we would need several photonic crystal designs to cover a wide momentum range and to separate between all the particles. However, unlike conventional radiators, a photonic crystal can be designed to cover any desired range, instead of being limited by the values of refractive indices available in nature.

(6.4) Equivalence between Cherenkov radiation of Bloch modes and resonance transition radiation

From the perspective of the *local* interaction between the charged particle and the layers constituting the photonic crystal, there will be two types of radiation processes, including the conventional Cherenkov radiation inside each dielectric layer and the transition radiation generated at each interface. For Fig. 1b, since the particle velocity is below the Cherenkov threshold at each dielectric material, there will be no conventional Cherenkov radiation inside each layer. For Figs. 3 and 4, since the generated conventional Cherenkov radiation inside each

dielectric has $k_\rho > \omega/c$, the conventional Cherenkov radiation will not contribute to the radiation in air but will be guided within the waveguide-like photonic crystal (due to total internal reflection). Therefore, in both Fig. 1b and Figs. 3 and 4, and generally in the designs we propose in this paper, the radiation into air comes *only* from the interference of transition radiation generated at each interface, i.e., resonance transition radiation.

The resonance transition radiation that interferes constructively in air, and the generation of Bloch modes that are allowed to couple out to air, become the same underlying process when the photonic crystal is sufficiently thick. They are just two equivalent perspectives of the same phenomenon resulting in radiation into air.

In order to gain an intuitive understanding, we may qualitatively analyze the radiation into air from the perspective of the interaction between the charged particle and the subset of Bloch modes that can couple out to air. (This is done by focusing on the discussion on Bloch modes with $k_\rho < \omega/c$, due to their capability of transmitting into air, while the Bloch modes with $k_\rho > \omega/c$ will stay trapped/guided within the photonic crystal.)

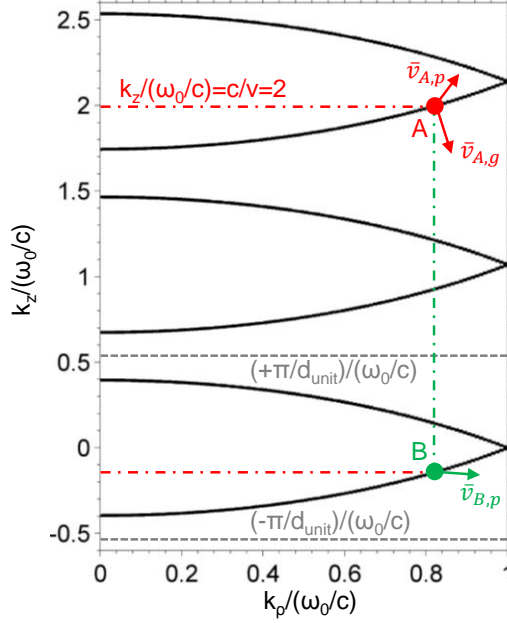
We can show that from the perspective of the radiation into air, the case above is equivalent to considering the photonic crystal as a *homogeneous* effective material with an effective (potentially nonlocal) permittivity and permeability. This way, we can effectively treat the total radiation into air as the superposition of two elements: (1) the generated Bloch modes transmitted into air (i.e., the effective Cherenkov radiation from photonic crystal) and (2) the transition radiation at the interface of air/*homogeneous* bulk. When the photonic crystal is sufficiently thick, the generated Bloch modes transmitted into air will dominate the whole radiation into air. Under this condition, the generated Bloch modes that couple out to air and the resonance transition radiation that constructively interfere in air are the same. It is thus reasonable to treat the resonance transition radiation that constructively interfere in air as the effective Cherenkov radiation from the photonic crystal.

(6.5) Phase velocity of excited Bloch modes that can couple out to air

In this section we use the photonic crystal in Fig. 1b to analyze the relation between the particle velocity and the phase velocity of the Bloch mode of photonic crystal being able to couple out to air. Supplementary Figure 9 shows the isofrequency contour of the photonic crystal at the wavelength of 700 nm for the range of $k_\rho \leq \omega/c$.

When the charge particle has a velocity of $\bar{v} = \hat{z}v$ ($v = 0.5c$), the charged particle excites Bloch modes with its

z-component wavevector being $k_{z,A} = \frac{c}{v} \cdot \frac{\omega}{c} = 2 \frac{\omega}{c}$ (denoted as eigenmode A in Supplementary Fig. 9). For eigenmode A, the z-component of group velocity $\bar{v}_{A,g}$ is antiparallel to the direction of motion of the particle, i.e., $\hat{z} \cdot \bar{v}_{A,g} < 0$; and the z-component of the wavevector is equal to ω/v , i.e., $k_A > k_{z,A} = \omega/v$. Therefore, $v > \omega/k_A = |\bar{v}_{A,p}|$; thus, we show that the phase velocity of the excited Bloch modes before the periodic modulation (denoted as $\bar{v}_{A,p}$ in Supplementary Fig. 9) is smaller than the particle velocity. However, it is worthy to note that the value of $k_{z,A}$ for the generated field of eigenmode A is modulated by the periodic structure, i.e., $k_{z,A} = k_{z,0,A} + m_A \frac{2\pi}{d_{unit}}$, where $|k_{z,0,A}| \leq \frac{\pi}{d_{unit}}$, m is an integer number, and d_{unit} is the thickness of unit cell of photonic crystal. For eigenmode A, its corresponding value of $k_{z,0,A}$ is negative (along with $m_A = -2$) and is the same as the value of the z-component wavevector $k_{z,B}$ for eigenmode B in Supplementary Fig. 9; for eigenmode B, we also have $k_{z,B} = k_{z,0,B} + m_B \frac{2\pi}{d_{unit}}$, where $k_{z,B} = k_{z,0,B}$ and $m_B = 0$. This way, when the generated eigenmode A propagates inside the photonic crystal, its phase velocity after the periodic modulation (denoted as $\bar{v}'_{A,p}$, not shown in Supplementary Fig. 9) will be different from that before the periodic modulation, i.e., $\bar{v}'_{A,p} \neq \bar{v}_{A,p}$; in contrast, it will be the same as that of eigenmode B, i.e., $\bar{v}'_{A,p} = \bar{v}_{B,p}$. That is why in Fig. 1b the z-component of phase velocity $\bar{v}'_{A,p}$ for the generated plane wave near the trajectory of the charged particle is also antiparallel to the direction of motion of the particle.



Supplementary Fig. 9 | Isofrequency contour of the photonic crystal. Here we focus on the Bloch modes with $k_\rho < \omega/c$ due to their capability to couple out to air. The wavelength is $\lambda_0 = 700$ nm and $\omega_0 = 2\pi c/\lambda_0$. The photonic crystal is the same as that in Fig. 1b, where the thickness of its unit cell is denoted as d_{unit} . The charged particle moves along the $+\hat{z}$ direction with $v = 0.5c$. The values of k_ρ are the same for eigenmodes A and B. The region with $|k_z| \leq \pi/d_{unit}$ denotes the first Brillouin zone.

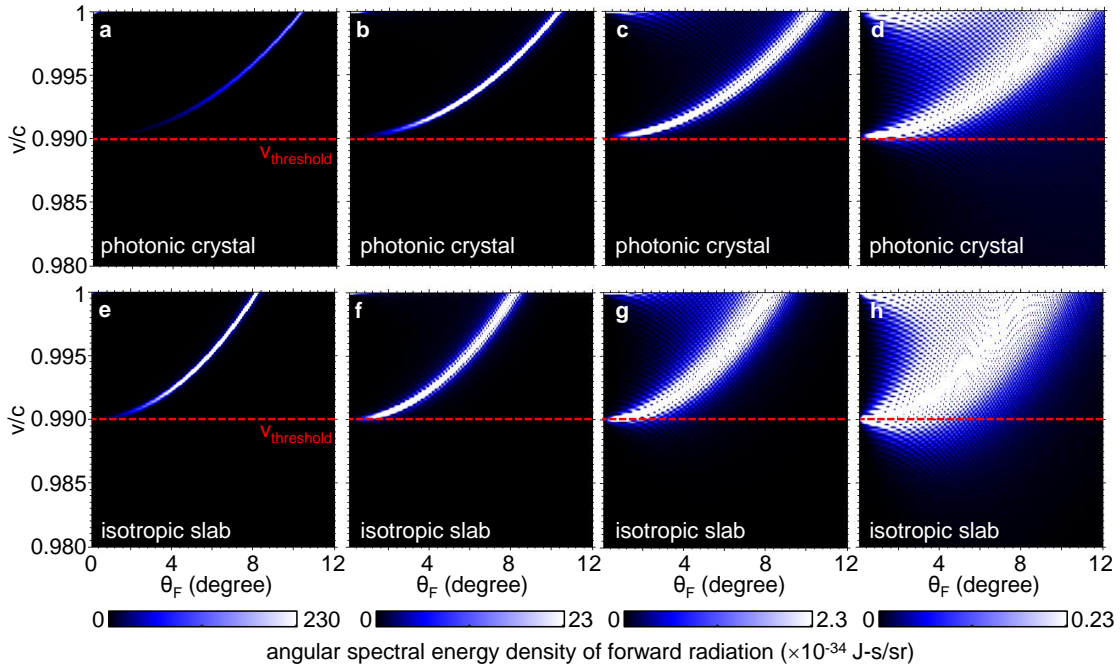
(6.6) Threshold of particle velocity for Cherenkov radiation from photonic crystals

All radiation into air in this paper comes only from the resonance transition radiation. Although the (regular) transition radiation has no threshold for the particle velocity, a resonance transition radiation that interferes constructively in air does have a threshold for the particle velocity $v_{threshold}$ (i.e. a cutoff). Because of the existence of this threshold, it is possible to distinguish two regimes for the radiation into air, i.e., Cherenkov-like radiation when $v > v_{threshold}$ and the transition-like radiation when $v < v_{threshold}$. The main topic of this paper is the Cherenkov-like radiation with $v > v_{threshold}$.

For example, the threshold for the particle velocity is $v_{threshold} = 0.99c$ for the case in Fig. 3a and Fig.4b. In order to clearly demonstrate this threshold, we re-plot Fig. 3a with a much wider range of particle velocities in Supplementary Fig. 10a-d. When $v < v_{threshold}$ ($v > v_{threshold}$), the resonance transition radiation will interfere destructively (constructively) in air, and the angular spectral energy density at the range of $v < v_{threshold}$ is much (~ 2 order of magnitude) smaller than that at the range of $v > v_{threshold}$; in addition, the

radiation into air is highly directional only when $v > v_{threshold}$. Therefore, the Cherenkov-like radiation into air is formed only when $v \geq v_{threshold}$, and the transition-like radiation appears when $v < v_{threshold}$.

To emphasize the Cherenkov-like behavior of the resonance transition radiation, note the similarity to radiation from a dielectric slab shown in Supplementary Fig. 10e-h. It is well known that the conventional Cherenkov radiation will dominate the whole radiation into air when $v > v_{threshold}$, and there is only the transition radiation when $v < v_{threshold}$. From the similarities between Supplementary Fig. 10a-d&e-h, it is safe to conclude that when $v > v_{threshold}$ ($v < v_{threshold}$) the radiation from photonic crystal into air is similar to the Cherenkov radiation (transition radiation) generated from a dielectric slab. Therefore, it is reasonable to treat the radiation from photonic crystal into air as the Cherenkov-like radiation when $v > v_{threshold}$.



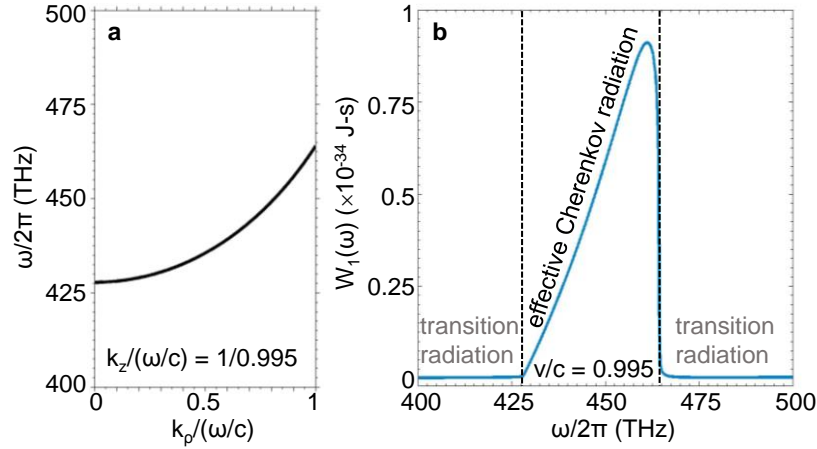
Supplementary Fig. 10 | Above- and below-threshold behavior for resonance transition radiation and Cherenkov radiation.

The panels show the angular spectral energy density of forward radiation $U_{N+1}(\omega_0, \theta)$ for different colorbar scales. In each panel, the red dashed line denotes the threshold of particle velocity. **a-d**, $U_{N+1}(\omega_0, \theta)$ from a photonic crystal. **e-h**, $U_{N+1}(\omega_0, \theta)$ from a dielectric slab. When $v > v_{threshold}$, the radiation near the Cherenkov angle (i.e., the effective or conventional Cherenkov radiation) dominates the whole radiation in air, and the radiation at other angles (i.e. transition radiation) is very minor. When $v < v_{threshold}$, the radiation in all angles (i.e. transition radiation) is very small. The photonic crystal here is the same as that in Fig. 3a. The dielectric slab has a hypothetical refractive index of 1.01 and a thickness of 2 mm. The wavelength is $\lambda_0 = 700$ nm and $\omega_0 = 2\pi c/\lambda_0$.

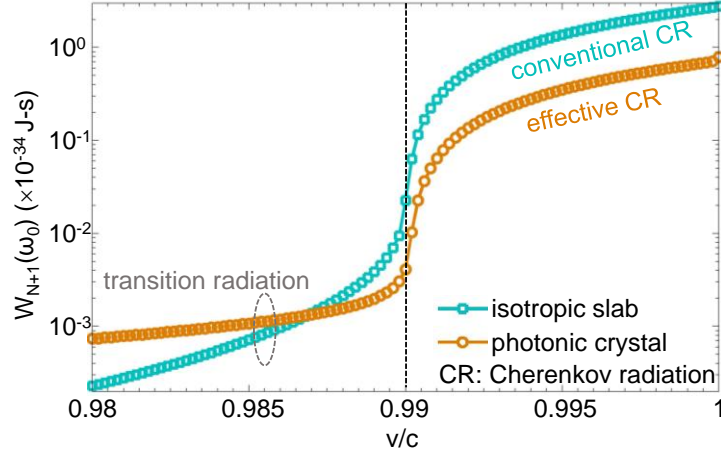
(6.7) Similarity between radiation spectra from a photonic crystal and from a dielectric slab

We show the radiation spectrum from photonic crystals at a fixed velocity in Supplementary Fig. 11 (with the example of the backward Cherenkov radiation in Fig. 4). Supplementary Figure 11 shows that when the photonic crystal has (does not have) Bloch modes that can couple out to air, the radiation into air is Cherenkov-like (transition-like). In addition, the radiation spectrum from each photonic crystal design has clear jumps between frequency ranges having either Cherenkov-like or transition-like radiation.

In addition, the spectra of forward radiation from a photonic crystal and from a dielectric slab at a fixed wavelength at different particle velocities are shown for comparison in Supplementary Fig. 12. A clear jump near $v = v_{threshold}$ is also found both in the radiation spectra from the photonic crystal and the dielectric slab. It is thus reasonable to argue that when $v > v_{threshold}$ ($v < v_{threshold}$), the radiation from photonic crystal into air is Cherenkov-like (transition-like) radiation.



Supplementary Fig. 11 | Backward Cherenkov radiation from photonic crystal at a fixed velocity of $v = 0.995c$, showing jumps between frequency ranges having either Cherenkov-like or transition-like radiation. a, Dispersion of Bloch eigenmodes of photonic crystal at a constant value of $k_z/(\omega/c) = c/v$. We focus on Bloch modes with $k_p < \omega/c$ since these are the only ones that can couple out to air. Such Bloch modes exist for this configuration in the range of [427.8 464] THz. **b**, Backward radiation spectrum $W_1(\omega)$. The frequencies at 427.8 THz and at 464 THz are denoted by the dashed lines to mark the jumps between Cherenkov-like and transition-like radiation. The photonic crystal’s layers are the same as in Fig. 4, and the number of periods is $M = 1000$. The radiation into air is a Cherenkov-like (transition-like) radiation inside (outside) the frequency range of [427.8 464] THz.

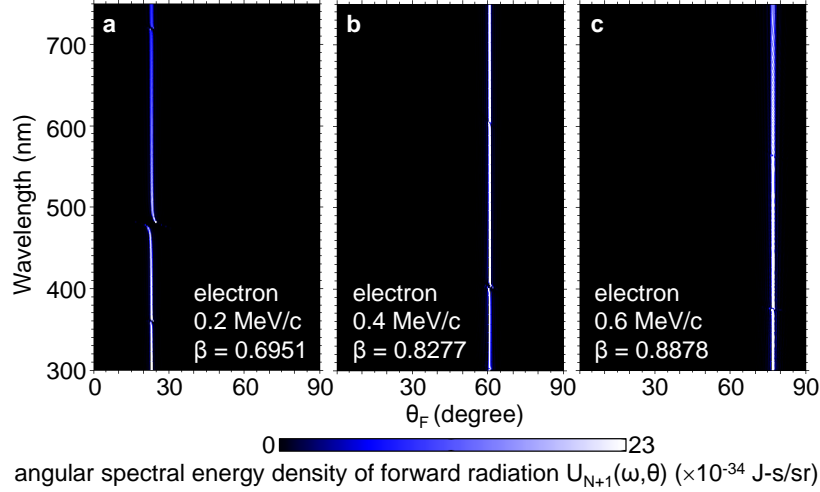


Supplementary Fig. 12 | Spectra of forward radiation $W_{N+1}(\omega_0)$ from a photonic crystal and from a dielectric slab at different particle velocities. Both contain a clear velocity threshold that shows that the radiation is Cherenkov-like. Here $W_{N+1}(\omega_0) = \int_0^{\pi/2} U_{N+1}(\omega_0, \theta) \cdot (2\pi \sin\theta) d\theta$ (see equation (74)), where $U_{N+1}(\omega_0, \theta)$ is shown in Supplementary Fig. 10. When $v > v_{threshold}$ ($v_{threshold} = 0.99c$, denoted as the dashed line), the resonance transition radiation interferes constructively in air, leading to the formation of effective Cherenkov radiation. The setup for this figure is the same as in Supplementary Fig. 10.

(6.8) Bandwidth and chromatic aberration correction of Cherenkov radiation from photonic crystals

For the effective Cherenkov radiation from a photonic crystal, the bandwidth is typically of the order of several hundred nm. In the various photonic crystal designs, the most important feature for particle identification is the high sensitivity to the particle velocity. This feature can be maintained over several tens to few hundreds of nm, depending on the specific photonic crystal design, the dielectric materials used, and the range of particle momenta selected. Although the effective Cherenkov radiation from the photonic crystal exists over a large bandwidth, it can be accompanied by a dispersion that causes chromatic aberrations. This dispersion is the direct outcome of the periodicity of the structure, and consequently, the effective Cherenkov angle from a given photonic crystal can vary with the wavelength. Such chromatic aberrations are also seen in other photonic crystal applications [54, 55]. To make use of the entire bandwidth available, one may need to compensate for the chromatic aberration or to minimize its impact on particle identification when designing the crystal structure.

In order to illustrate that the chromatic effect depends on the photonic crystal design, an example configuration for a photonic crystal is considered in Supplementary Fig.13. The angular spectral densities for three different particle velocities are shown in the wavelength range 300-750 nm. It can be inferred that, for this structure in Supplementary Fig.13, there is negligible chromatic effect in the wavelength range shown.



Supplementary Fig. 13 | Broadband effective forward Cherenkov radiation from photonic crystals. One can see a clear Cherenkov signal produced in the wavelength range of 300-750 nm, with a negligible dispersion. The value of $\beta = v/c$ is 0.6941 in **a**, 0.8277 in **b**, and 0.8878 in **c**, respectively. The particle used here is the electron and its momentum is denoted in each panel. The photonic crystal consists of 250 periods (i.e., 500 layers); the thickness of each layer is 250 nm; and the refractive indices are $n_1 = 1.414$ and $n_2 = 1.567$, respectively.

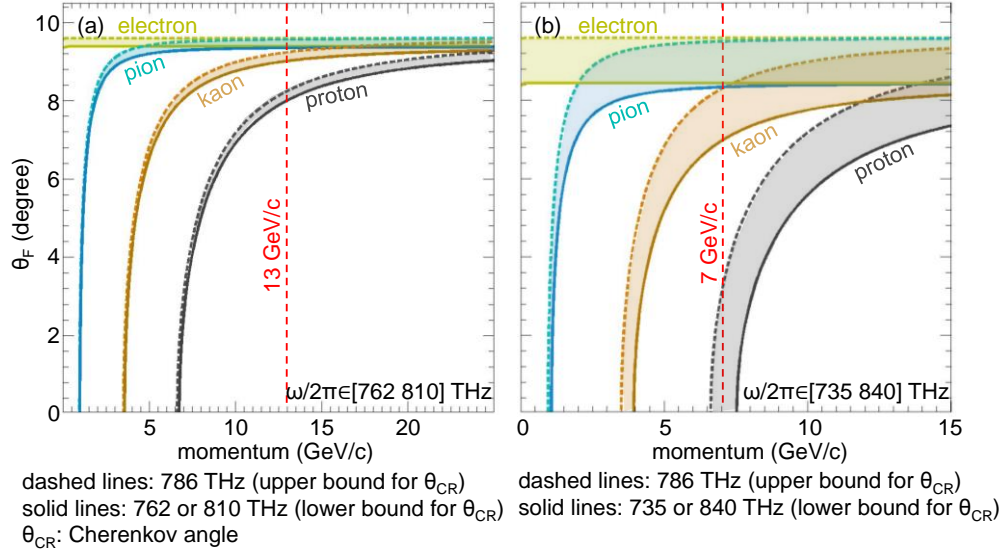
When designing the photonic crystals which have chromatic aberration, some of the options for mitigating the influence of these aberrations on particle identification are discussed below.

- (a) A simple option is to limit the frequency range used in signal detection, using optical filters. In order to compensate for the reduction in signal due to the limited bandwidth, one may increase the number of layers. Another similar option is to keep the broader frequency range detection but instead limit the maximum momentum envisaged for particle identification from a given photonic crystal structure, thus increasing the angular separation between the particles and consequently reducing the effect of chromatic aberrations. For example, for the photonic crystal structure used in Fig. 3c, using a bandwidth of 6 THz, the ranges of Cherenkov angle for pion, kaon and proton are well separated below 3 GeV/c; see Supplementary Fig. 15a below.
- (b) The chromatic error from the dispersion of refractive index exists for Cherenkov radiation from conventional radiators also. In some detectors, the Cherenkov photons travel for couple of meters before they are focused on the photon detector plane. As described in Ref. [40], one of the techniques

that has been tried is to measure the time of arrival of photons on the detector plane, in addition to their spatial coordinates. This method makes use of the fact that, photons with larger wavelengths have relatively larger group velocity and thus arrive at the detector plane earlier, than the photons of lower wavelengths produced by the same charged track. Hence after performing appropriate calibration of the setup, the time of arrival of the photons from a charged track can be used to infer the corresponding photon wavelengths and thus apply the corresponding corrections to the Cherenkov angles. This method can be applied to the Cherenkov radiation from photonic crystals to increase the usable bandwidth.

- (c) A different but innovative and more general approach is to integrate chromatic aberration correction as part of the design of the photonic crystal structure. One option is to use gain materials with anomalous dispersion to construct the photonic crystals, since the material's anomalous dispersion can help to cancel out the dispersion caused by the periodic structure. Supplementary Figure 14a shows that the photonic crystals based on gain materials with anomalous dispersion are suitable for particle identification with a relatively wide frequency bandwidth of 48 THz, even for particle momentum range of 1-16 GeV/c. For example, when the particle momentum is 13 GeV/c in Supplementary Fig. 14a, the angular ranges of Cherenkov radiation for pion, kaon and proton are $[9.4^\circ \text{ } 9.6^\circ]$, $[9^\circ \text{ } 9.2^\circ]$, and $[8^\circ \text{ } 8.2^\circ]$, respectively, which are well separated and can enable the different particle types to be effectively distinguished from one another. Moreover, the working bandwidth can be extended to above 100 THz when the particle momentum is below 10 GeV/c, such as the case of 7 GeV/c shown in Supplementary Fig.14b. Anomalous dispersion can exist in materials with gain (e.g., [41-43]) and in materials with loss. Usage of materials with gain for chromatic correction, avoids the problem of potential photon propagation loss associated with other materials which may also offer anomalous dispersion. The usage of such gain materials may also help to design thin Cherenkov radiators with a high photon yield, since the photons emitted will be amplified during their propagation. Moreover, the anisotropy in the direction normal to the particle path may also help to magnify the Cherenkov angles produced [14], which in turn would separate out the plots similar to those shown in Supplementary Fig. 15a and reduce the effect of the chromatic aberration. Alternately, the usage of optical elements (such as the achromatic

doublet) to apply chromatic aberration corrections, as done in many microscopes [44, 45, 56, 57], is also worth exploring.



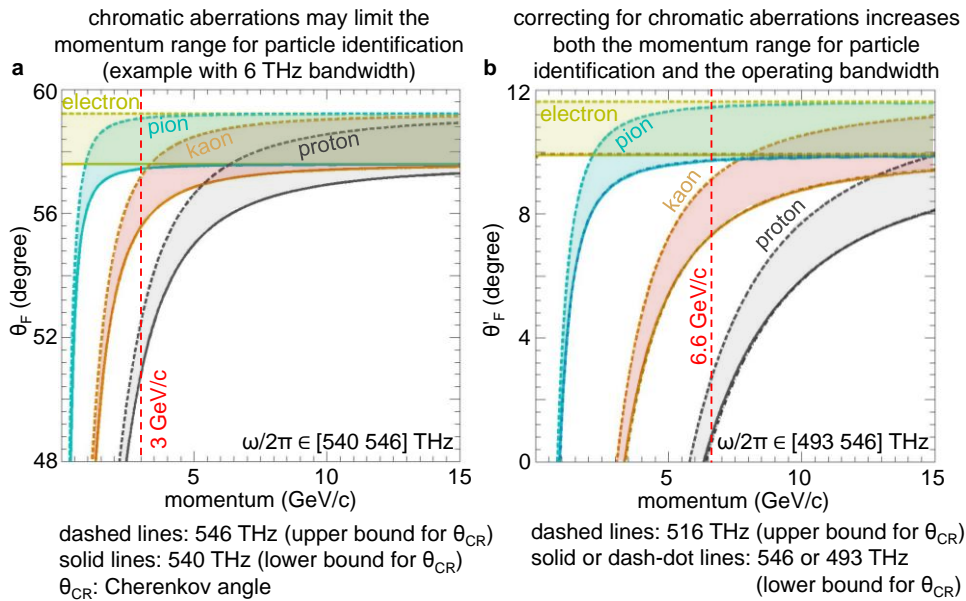
Supplementary Fig. 14 | Cherenkov angle versus particle momentum from photonic crystal assembled using a material with anomalous dispersion. This figure shows the forward Cherenkov angles from different types of particles as a function of their momenta, within the frequency range (a) of [762 810] THz and (b) of [735 840] THz. The shaded region of each particle denotes the angular range in which Cherenkov radiation can be emitted within the chosen frequency range. The corresponding wavelength range is [370 394] nm in (a) and [357 408] nm in (b). The photonic crystal configured here is suitable for particle identification for a momentum up to 16 GeV/c in (a) and up to 10 GeV/c in (b). For example, when the particle momentum is 13 GeV/c, the angular range of Cherenkov radiation in (a) is [9.4° 9.6°], [9.4° 9.6°], [9° 9.2°], [8° 8.2°] for electron, pion, kaon and proton, respectively. When the particle momentum is 7 GeV/c, the angular range of Cherenkov radiation in (b) is [8.4° 9.6°], [8.3° 9.5°], [7° 8.3°], [0° 3.1°] for electron, pion, kaon and proton, respectively. For this photonic crystal, the thickness of unit cell is $d_{unit} = 2 \mu\text{m}$; within each unit cell, the thickness of each of the two dielectric constituents are $d_1 = d_2 = 0.5d_{unit}$; $\epsilon_{r1} = 1.97$, and $\epsilon_{r2} = 4 - 0.4\omega/(2\pi c/d_{unit})$. Within the chosen frequency range, ϵ_{r2} varies by 0.13 in (a) and of 0.28 in (b). Such small variations of ϵ_{r2} , are typical in gain materials (e.g., [40-42]) with anomalous dispersion. For this illustration, the imaginary part of ϵ_{r2} is neglected.

In order to test the potential of these approaches, we performed numerical simulations to optimize a simple aberration correction consisting of a linear frequency dependent shift to the angle. The results are shown in Supplementary Figs. 15 and 16. For comparison, Supplementary Fig. 15a is created without the chromatic correction for a frequency range of 540-546 THz, where overlaps can be seen between the plots for different particle types above 3 GeV/c. In contrast, Supplementary Fig. 15b is created after chromatic aberration correction for a frequency range of 493-546 THz, exhibiting reduced overlaps. For example, in this figure, even at 6.6 GeV/c, the variation of the Cherenkov angles due to dispersion are in the ranges [9.7°, 11.4°], [7.3°, 9.1°] and [0.8°, 2.7°] for pion, kaon and proton, respectively and thus these particle types can be distinguished from one another. The corresponding angular radiation spectra are shown in Supplementary Fig. 16. The example linear

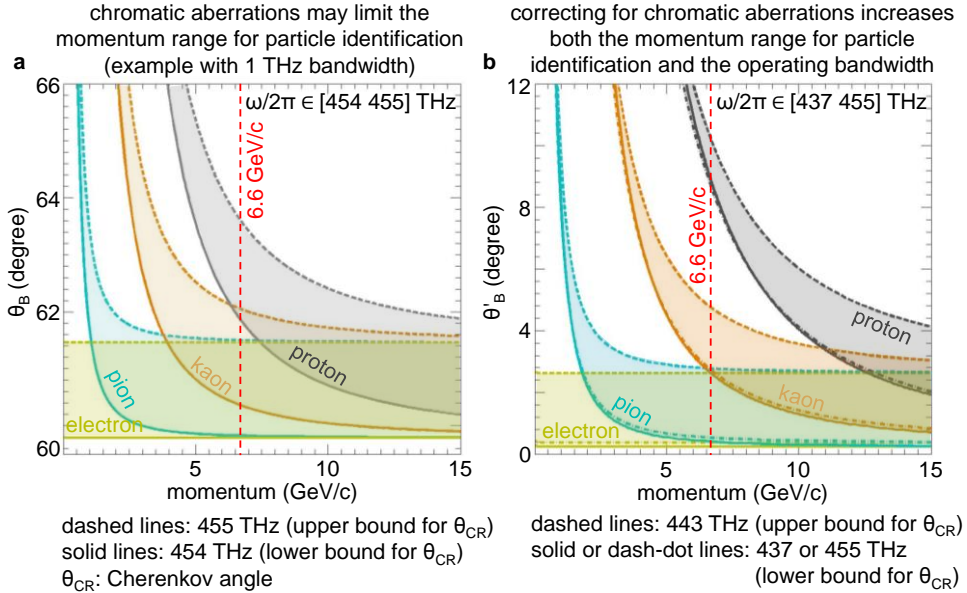
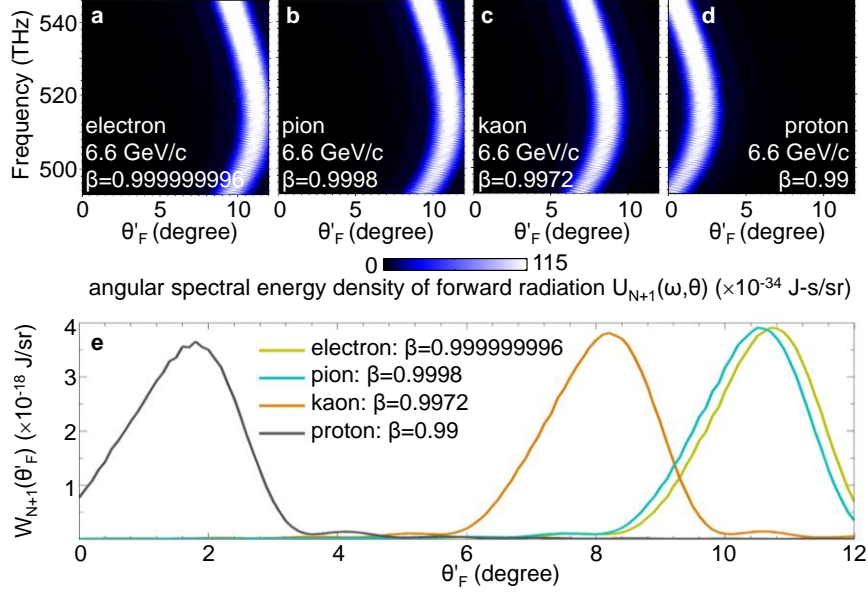
chromatic aberration correction applied here enables to expand the operating bandwidth from 6 THz to 53 THz and to augment the upper momentum limit for particle identification from 3 to approximately 7.5 GeV/c while maintaining the sensitivity to particle velocity.

The same exercise is repeated for backward Cherenkov radiation in Supplementary Fig. 17, which show the plots of Cherenkov angle vs momentum before and after applying a similar simple correction. The corresponding angular spectral energy densities are shown in Supplementary Fig. 18.

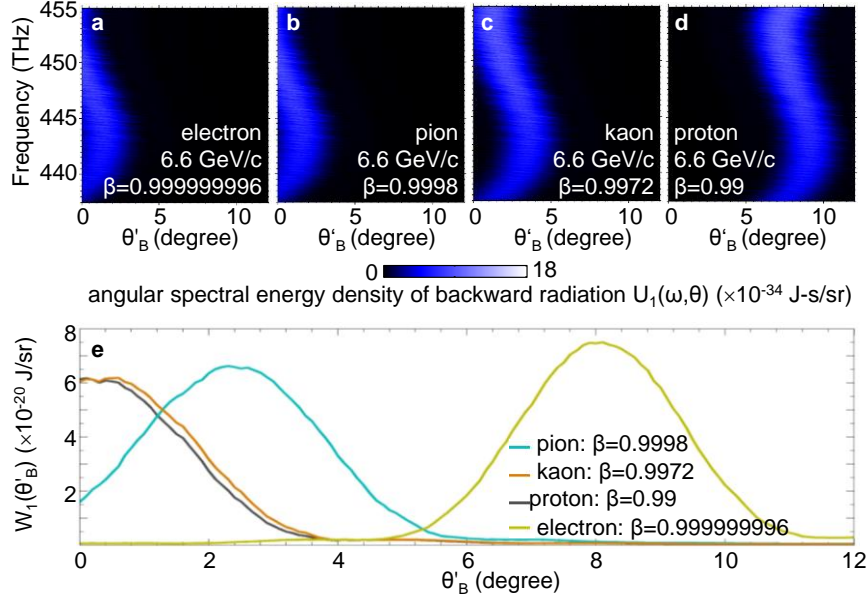
We also note that correcting for chromatic aberrations is part of optimizing the design of photonic crystal as a radiator and one may use a mixture of the solutions described above.



Supplementary Fig. 15 | Particle identification using photonic crystal as radiator: with and without chromatic aberration correction. The two panels show the Cherenkov angles of forward Cherenkov radiation versus particle momenta for a certain frequency range (a) before and (b) after a chromatic aberration correction. The photonic crystal here is the same as that in Fig. 3a. For the chromatic aberration correction, a linear function of $\theta'_F = 6\theta_F - \frac{12}{7} \left(\frac{\omega/2\pi}{1\text{THz}} - 344.2 \right) \cdot 1\text{degree}$ is applied between the original radiation angle θ_F and the post-processed radiation angle θ'_F . The shaded region of each particle denotes the angular range to which Cherenkov radiation is emitted within the chosen frequency range. Applying the aberration correction results in the shaded regions for pion, kaon and proton becoming more separated from each other. The corresponding wavelength range in b is [549.5 608.5] nm.



momentum of 6.6 GeV/c, the range of Cherenkov angles for pion (or electron), kaon and proton are well separated from (overlapped with) each other after (before) chromatic aberration correction. The corresponding wavelength range in **b** is [659.3 686.5] nm.



Supplementary Fig. 18 | Angular distribution of backward Cherenkov radiation from a photonic crystal. a-d, Angular spectral energy density $U_1(\omega, \theta)$. **e**, Angular radiation spectra $W_1(\theta) = \int_{\omega_{min}}^{\omega_{max}} U_1(\omega, \theta) d\omega$. This figure shows that even at momentum of 6.6 GeV/c, despite the chromatic aberration angular broadening, pion (or electron), kaon and proton are still distinguishable after applying a chromatic aberration correction. The correction applied is the same as that in Supplementary Fig. 17b. Here, the photonic crystal's layers are the same as in Fig. 4a. A number of periods of $M = 1000$ is chosen.

(6.9) Angular spectral energy density and the radiation spectrum at a fixed velocity

For the forward Cherenkov radiation, the angular spectral energy density and the angular radiation spectra at four different fixed velocities are shown in Supplementary Fig. 16a-d and Supplementary Fig. 16e, respectively, with the same example of chromatic aberration correction described above. Similarly, for the backward Cherenkov radiation, the angular spectral energy density and the angular radiation spectra at four different fixed velocities are shown in Supplementary Fig. 18a-d and Supplementary Fig. 18e, respectively.

(6.10) Fraction of Cherenkov radiation emitted into the desired direction

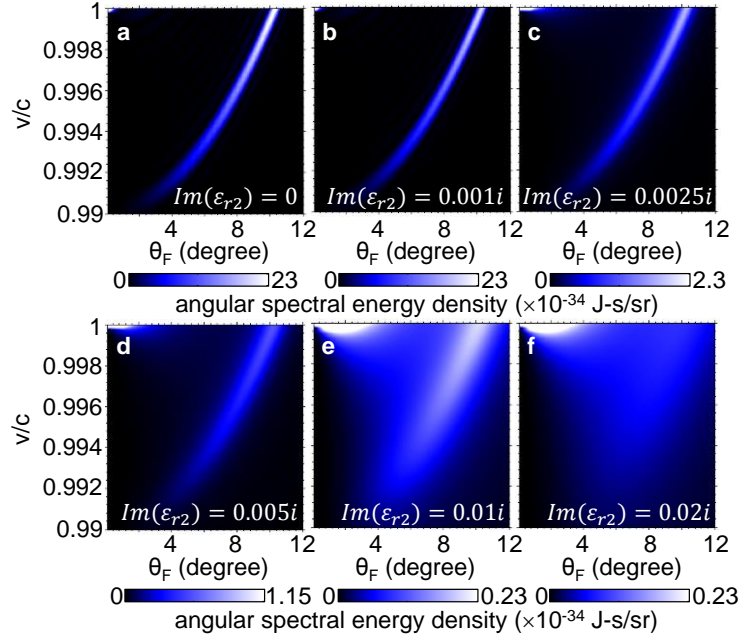
The fraction of Cherenkov radiation emitted in the desired direction, which is defined as $\eta = \frac{\int_{\theta_{min}}^{\theta_{max}} W_{N+1}(\theta) d\theta}{\int_0^{\pi/2} W_{N+1}(\theta) d\theta}$,

where $[\theta_{min} \theta_{max}]$ is the range of Cherenkov angles within the chosen frequency range. The value of η is over 75% for both the forward and backward Cherenkov radiation. For example, $[\theta_{min} \theta_{max}]$ are $[9.9^\circ, 11.6^\circ]$, $[9.7^\circ,$

11.4°], [7.3°, 9.1°] and [0.8°, 2.7°] for electron, pion, kaon and proton, respectively, at 6.6 GeV/c in Supplementary Fig. 15b. Over 75% of the Cherenkov radiation emission is contained within these ranges of Cherenkov angles (Supplementary Fig. 16e). The value of η can be further improved by using a thicker photonic crystal, since the angular spread of Cherenkov radiation decreases when the thickness of photonic crystal increases; see more information on this topic in Supplementary Fig. 8.

(6.11) Impact of material loss on Cherenkov radiation from photonic crystal

The material loss indeed has a detrimental impact on the performance of all Cherenkov detectors, since it reduces the signal and destroys the relation between Cherenkov angle and particle velocity by significantly broadening the angle-velocity relation. Therefore, it shall be necessary to use materials that are nearly-purely transparent (such as the proposed photonic crystals based on transparent dielectrics in this work) to gain efficient control of Cherenkov angles. We further check the impact of material loss on Cherenkov radiation from photonic crystals in Supplementary Fig. 19, by considering the realistic values of loss and comparing them with results obtained after using values that are artificially increased. To exhibit the dependence on loss, Supplementary Fig. 19 shows that when the material loss increases, the relation between Cherenkov angle and particle velocity will also disappear, similar to what happens in metal-based metamaterials (with a complex permittivity) in Supplementary Fig. 5. However, importantly, realistic values of loss in realistic transparent dielectric are low enough to yield results that are equivalent to having no loss at all.



Supplementary Fig. 19 | Impact of loss in material, on the angular spectral energy density of forward radiation from photonic crystals. The wavelength is 700 nm. The photonic crystal's layers are the same as in Fig. 3a. The number of periods in the photonic crystal is $M = 1000$. The relative permittivity of the two dielectric constituents are $\epsilon_{r1} = 10.6$ and $\epsilon_{r2} = 2.1 + i \cdot Im(\epsilon_{r2})$, respectively. The value of $Im(\epsilon_{r2})$ is indicated in each figure.

Supplementary section 7: Production and usage of photonic crystals

(7.1) Feasibility of photonic crystal production

For photonic crystals, one can deposit layers so that the required thickness of each layer can be attained with single-nanometer precision (e.g., [49]). These techniques have already been performed by the industry over large areas (tens of cm^2 , e.g. [50, 58]), and the processes can be extended to much larger areas. Another approach that gives us both large area samples and large numbers of layers is by stretching polymers (e.g., [46-48, 59, 60]), which can provide meter-scale samples with thousands to tens of thousands of layers.

As for curved photonic crystals, some options for producing flexible photonic crystals are described in Ref.[46-48]. Finally, conventional layer deposition methods and optical lithography methods could be modified and re-optimized to work on curved (e.g., spherical) surfaces.

(7.2) Photon yield from photonic crystals:

The number of photons emitted per unit length from the photonic crystal described in this paper is similar to that from anisotropic metamaterials in Ref. [14], but is one order of magnitude smaller than what could be achieved from an isotropic material of hypothetical similar refractive index as can be inferred from Fig. 3a and Supplementary Sections 3 and 4. From a practical perspective, one may improve the total photon yield through further structural optimization, through increasing the thickness of photonic crystals, or through the using of 2D or 3D photonic crystals [30]. Using 2D and 3D photonic crystals also suggests the possibility of additional mechanisms for the enhancement of Cherenkov radiation, such as the excitation of modes with high density of states at points of van-Hove singularities [20, 61].

Supplementary References

- [51] Yamada, K., Hosokawa, T. & Takenaka, H. Observation of soft x rays of single-mode resonant transition radiation from a multilayer target with a submicrometer period. *Phys. Rev. A* **59**, 3673 (1999).
- [52] Chew, W. C. *Waves and Fields in Inhomogeneous Media* (IEEE Press, 1995).
- [53] Alves Jr., A. A. et al. (LHCb Collaboration), The LHCb Detector at the LHC. *J. Instrum.* **3**, S08005 (2008).
- [54] Ferrando, A., Silvestre, E., Miret, J. J. & Andres, P. Nearly zero ultraflattened dispersion in photonic crystal fibers. *Opt. Lett.* **25**, 709-792 (2000).
- [55] Ferrando, A., Silvestre, E., Andres, P., Miret, J. J. & Andres, M. V. Designing the properties of dispersion-flattened photonic crystal fibers. *Opt. Exp.* **9**, 687-697 (2001).
- [56] Kang, S. B. Chromatic aberration correction. U.S. Patent 7792357 (2010).
- [57] Torok, E. J. & Harvey, W. A. Chromatic aberration correction in a multiwavelength light beam deflection system. U.S. Patent 4435041 (1984).
- [58] Zhurin, V. V., Kaufman, H., Kahn, J. R., & Hylton, T. L. Biased target deposition. *J. Vac. Sci. Technol. A* **18**, 37-41 (2000).
- [59] Ponting, M., Hiltner, A. & Baer, E. Polymer nanostructures by forced assembly: Process, structure, and properties. *Macromol. Symp.* **294-I**, 19-32 (2010).
- [60] Shen, Y. et al. Structural Colors from Fano Resonances. *ACS Photon.* **2**, 27-32 (2015).
- [61] Kremers, C., Chigrin, D. N. & Kroha, J. Theory of Cherenkov radiation in periodic dielectric media: Emission spectrum. *Phys. Rev. A* **79**, 013829 (2009).